Electronic Supplementary Information

Facile, Shear-Induced, Rapid Formation of Strong Gels of Chitosan through *In Situ* Generation of Colloidal Metal Salts

I. Experimental

a. Materials

Chitosan was procured from R.K. Scientific Company, Chennai. It had a weight average molecular weight (MW) of 51 kDa and a polydispersity of 1.05, as determined through GPC measurements, using PEG standards. The degree of deacetylation was calculated to be 80 %, based on FTIR measurements. All other reagents, including the metal salts, used were of an analytical grade and used, without any additional purification step. Distilled water was used for all the experiments. Diallylamine and acrylamide, utilized for the aza-Michael addition were also of an analytical grade (Purity > 99 %) and obtained from Sigma-Aldrich, India and Sisco Research Laboratories Pvt. Ltd. They were directly used, without any additional purification step.

Biological reagents, used for cell culture experiments, such as DMEM media (Dulbecco's Modified Eagle Medium), 10% (v/v) Fetal Bovine Serum (FBS), 1% (v/v) penicillin, streptomycin, trypsin/EDTA and Phosphate Buffer Saline pH 7.4 (PBS) were purchased from Gibco, India. NIH 3T3 mouse fibroblast cells were purchased from ATCC, Pune. Other reagents such as thiazolyl blue tetrazolium bromide ($C_{18}H_{16}BrN_5S$), sodium hydroxide (NaOH) and dimethyl sulfoxide (DMSO) were purchased from Sigma-Aldrich, India. HPLC grade water and ethanol was purchased from Merck, India. For the biological applications alone, high molecular weight chitosan (Purity > 99 %, Degree of Deacetylation-90 %, Viscosity-800 mPa.s) from Sisco Research Laboratories Pvt. Ltd. was utilized, for the preparation of the gels.

b. Preparation of the gels

Among the many possible variants, gels out of metal phosphates were chosen as the model. Gelation was carried out, preferably, in a plastic container. To about 50 ml of 2.5 w/v % chitosan solution in 2.5 v/v % acetic acid, a measured quantity of the metal salt was added, followed by the addition of a measured volume of a saturated, aqueous solution of the phosphate salt. Subsequently, the plastic container was sealed and the contents were vigorously shaken for few seconds to produce the gels. These gels were then extracted for further studies.

The molar ratios of the constituents of the Al^{3+}, Fe^{3+} and Ce^{4+}-based gels were optimized using steady state rheology. The constituents of the optimized cerium, ferric and aluminum-based gels are presented in Table S1.

Table S1. Constituents of the optimized cerium, ferric and aluminum-based gels.

Gel System	Chitosan Solution	Water Soluble Metal Salt	Satd. $(NH_4)_2HPO_4$ Solution
Ce (IV)	50 ml	1.28 g (CAN)	2 ml
Fe (III)	50 ml	0.16 g ($Fe(NO_3)_3.9H_2O$)	1 ml
Al (III)	50 ml	0.80 g (Anhy. $AlCl_3$)	3 ml

In the case of other gels, however, they were prepared by adding 300 µl of saturated aqueous solution of $(NH_4)_2HPO_4$ to a mixture of 5 ml of chitosan solution (2.5 w/v % in 2.5 v/v % acetic acid) and 100 mg of water-soluble metal salt and sheared well.

c. Characterization

Rheological and Chemical Characterization

Rheological response of the prepared gels was analyzed using steady and oscillatory shear rheological measurements on an Anton Paar Modular Compact Rheometer (MCR 102), equipped with a P-PTD 200/AIR Peltier temperature device. Parallel Plate 20 (PP 20) geometry was utilized for all the measurements, which were performed with a measurement gap of 1 mm. Prior to the measurements, the samples were equilibrated for 2 minutes. Solid state ^{13}C, ^{31}P and ^{27}Al Cross Polarization-Magic Angle Spinning (CP-MAS) Nuclear Magnetic

Resonance (NMR) spectra were recorded using a Bruker Avance spectrometer (^{1}H: 400 MHz), calibrated for all the nucleus using bromine signal from KBr. While the -CH_3 peak from N-acetyl group in chitosan was considered to be the internal reference in ^{13}C NMR (23.3 ppm), the ^{31}P peaks were calibrated by adding triphenyl phosphonium iodide as the external reference (29.33, 28.17 and 25.75 ppm). Infrared spectroscopy was performed using Jasco 4100 spectrometer. XRD analyses were performed using Bruker D8 advance Powder X-ray Diffractometer (PXRD), using Cu Kα as the x-ray source (λ = 1.54 Å). TGA was performed using TA Instruments Q500 Hi-Res TGA, with a heating rate of 20 °C min^{-1}, under N_2 flow. SEM imaging and elemental mapping of the surface was done under high vacuum using Hitachi S4800 Scanning Electron Microscope (SEM), fitted with energy dispersive X-ray (EDX) detector, after sputter coating with gold for 60 s. Electron Spin Resonance (ESR) spectra was recorded using Jeol JES FA200 spectrometer using an X- Band frequency of 9.45 GHz at room temperature (RT). Zeta potentials and size distribution of the various *ex situ* colloidal metal salts were determined using zeta sizer (Malvern Instruments-UK). High resolution mass spectrometry was performed using Micromass Q-TOF mass spectrometer, using water as the solvent.

After the preparation of the absorbents, water and saline absorption study was performed to study the free absorption capacity. In these measurements, around 100 mg of the sample was taken in a filter cone and immersed into a beaker containing distilled water or saline (0.9 wt. % NaCl solution). At the desired time intervals, the filter cone was taken out and weighed, after allowing excess water to drain for a period of 5 minutes. Apart from the free water absorption, absorption under load (AUL) test was also performed to determine the suitability as an absorbent in disposable sanitary napkins. For the same, an in-house test set-up was utilized. On one end of a PVC pipe, having an outside diameter of 25.4 mm and a wall thickness of 2 mm, a poly(propylene) mesh was glued using a commercial sealant. About 100 mg of the sample to be analyzed was loaded into the PVC pipe and a load of 160 g (Pressure of 50 g/cm^2) was introduced onto the sample by using a closely fitting glass vial, filled with mercury. Now, the test set-up was lowered into the saline solution and the water uptake was measured after 1 hour. A schematic of the in-house set-up is presented in Figure S1. Apart from the water uptake studies under different conditions, antimicrobial activity of the crosslinked product was also analyzed. These gels were tested against two different human pathogens; *Staphylococcus aureus* (gram +ve) and *Escherichia coli* (gram -ve). Muller Hinton Agar plates were used to

measure the inhibitory activity of the given compounds, which were used in different concentrations. Streptomycin was used as positive control.

Biological Studies

In vitro cytotoxicity was evaluated by MTT (3-(4,5-dimethylthiazol-2-yl)-5-(3-carboxylmethoxyphenyl)-2-(4-sulfophenyl)-2H-tetrazolium) assay method.[1] A mouse fibroblast cell line, NIH 3T3, was cultured using DMEM media with 10% FBS and incubated at 37 °C, 5 % CO_2 and 95 % relative humidity. Around 80% confluent cells were harvested using trypsin/ EDTA solution, resuspended at a density of $2*10^4$ cells per well and seeded into a 96 well tissue culture plate. Then, 80-90% confluency of the cells was achieved by incubating the plate for 24 h. In order to have control over the concentration of the scaffolds, they were finely pulverized using liquid N_2, and used. 100 µl /well of the three different concentrations, 0.1, 0.5 and 1 mg/ml, of powdered scaffolds, were added to the cultured cells in the 96 well plate. The cells were then incubated for 24 h, 48 h and 72 h with the media, for assessing the possible cytotoxicity. Cell viability was normalized to that of cells cultured only in media. After 24 h incubation, the media was removed, washed with PBS and 100 µl of MTT solution (0.5 mg/ml) was added to each well. The plate was incubated for 3 h and then MTT solution was removed. Subsequently, 100 µl of DMSO solution was added to dissolve the formazan crystals and again incubated for 10 minutes. After the incubation, the absorbance was measured at 570 and 670 nm using a microplate reader. $A_{570\ nm} - A_{670\ nm}$ was calculated to assess the cell viability.

For cell attachment studies using SEM, the UV sterilized scaffold was soaked with 100 µl of DMEM complete medium for 24 h. Then, the media was replaced and 100 µl of NIH 3T3 fibroblast cells, of concentration $2*10^4$, was added onto the scaffold. Cells were allowed to attach and proliferate for more than 24 h. Subsequently, cells were fixed with 4% HCHO. After fixing, HCHO was removed and rinsed with PBS thrice. It was followed by serial dilution of ethanol to dehydrate the scaffolds. Then, the scaffolds were gold sputtered for 190 seconds, prior to imaging by SEM analysis.

Nuclear integrity of intact cells, seeded onto the scaffolds was observed using 4',6-Diamidino-2-Phenylindole (DAPI) staining. In brief, the above scaffolds were seeded with 10^4 cells and incubated at 37 °C for 24 h. After removing the media and washing with PBS, 100µl of 4% formaldehyde was added to fix the cells for 10 min. After a PBS wash, the cells were permeabilized using Triton-X for 2 min. PBS wash was then repeated 4 more times and 100µl

of DAPI stain added and incubated for 10 min. Finally, the stain was removed, washed and replaced with PBS. Stained cells were visualized and imaged under UV light in fluorescence microscope.[2]

d. Cerium Gel-Catalyzed aza-Michael Addition

For aza-Michael addition, 2.08 ml (16.8 mmol) of diallylamine was taken in a round bottom flask, containing 100 ml of water. To the same, 1 g of acrylamide (14.1 mmol) was added and stirred well until dissolution. Subsequently, 0.5 g of the completely washed cerium-based, freeze-dried gel was added into the round bottom flask. Then, the reactants were stirred at room temperature for a period of 2 hours for the reaction to occur. Subsequent to the reaction, the heterogeneous catalyst was recovered by filtration and the product was separated by distillation under vacuum. The formation of the addition product was confirmed using multinuclear solution NMR spectroscopy and HR-ESI mass spectrometry.

II. Results and Discussion

Rheological Measurements

Cerium-based gel was taken as the model system to study the rheological properties. The optimum molar ratio of the gel precursors, ceric ammonium nitrate (CAN) and $(NH_4)_2HPO_4$, with respect to chitosan, was arrived at by studying the gel-strength using the steady shear rheological measurements. As the molar ratio of CAN was increased, the shear strength and the viscosity increased. However, at ratios higher than 0.3, the gel became very brittle. On the other hand, increase in the molar ratio of $(NH_4)_2HPO_4$, initially increased the strength and viscosity while beyond a ratio of 1, the same decreased. At even higher molar ratios, above 1.5, the gel began to drain out large quantities of water, which consequently increased the gel strength. Hence, molar ratios of 0.3 and 1 for CAN and $(NH_4)_2HPO_4$, with respect to chitosan, were chosen as the optimum. The shear stress (τ) versus shear rate ($d\gamma/dt$) plots for optimization of CAN and $(NH_4)_2HPO_4$, are given in Figures S1 and S2, respectively.

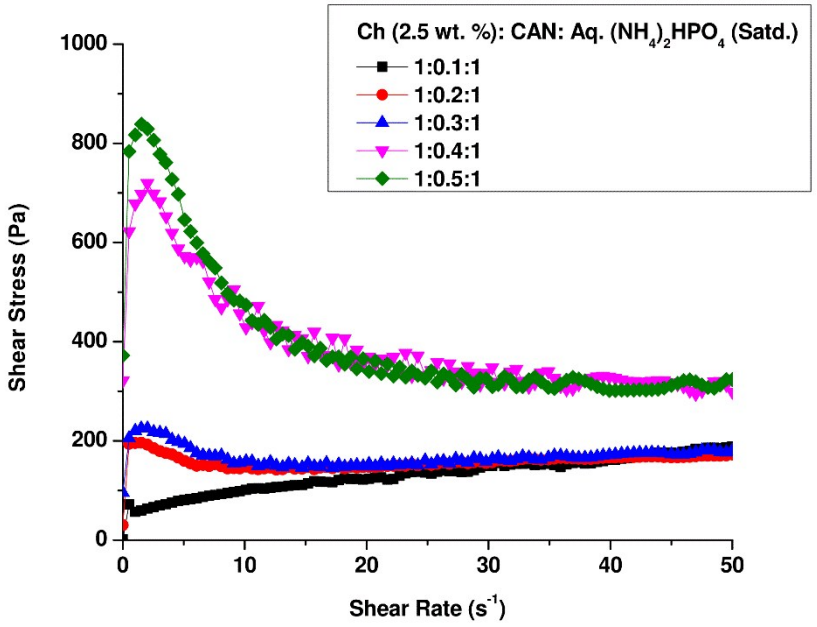

Figure S1. Steady shear measurements (shear stress vs. shear rate) for optimization of gelation with CAN.

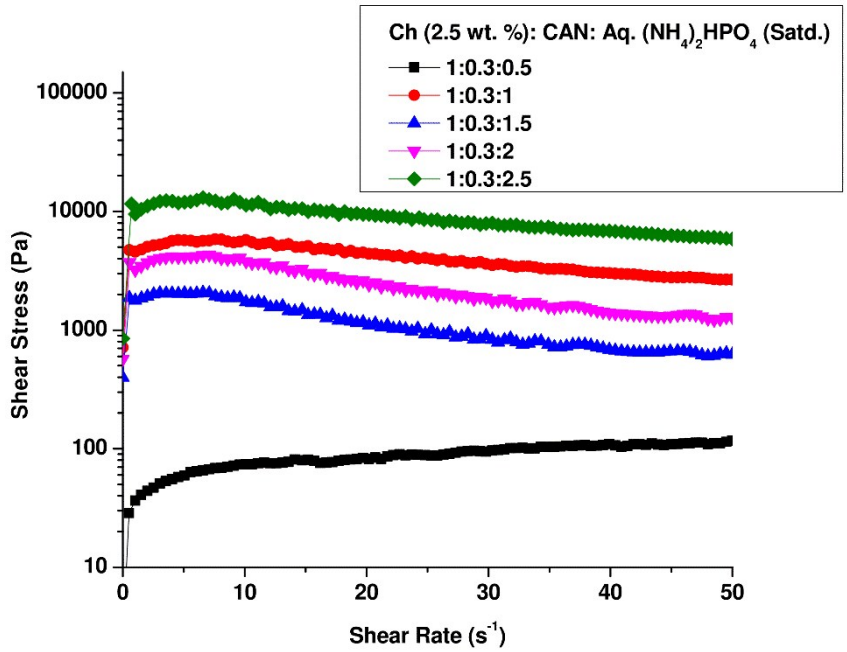

Figure S2. Steady shear measurements (shear stress vs. shear rate) for optimization of gelation with $(NH_4)_2HPO_4$.

The oscillatory shear rheological measurements were performed on the optimized gel to study the stability under an oscillatory shear. At a frequency of 1 Hz, under low shear strain, the storage modulus (G') dominated the loss modulus (G") by almost an order of magnitude, which is a characteristic of a visco-elastic gel. The gel was stable up to 13 % shear strain, beyond which G" began to dominate G'. At a shear strain of 0.1 %, which lied in the linear regime, the gel was stable throughout, between the measured interval. The strain sweep (ν = 1 Hz) and the frequency sweep (γ = 0.1) for the Cerium-based chitosan gel are presented in Figures S3 and S4, respectively.

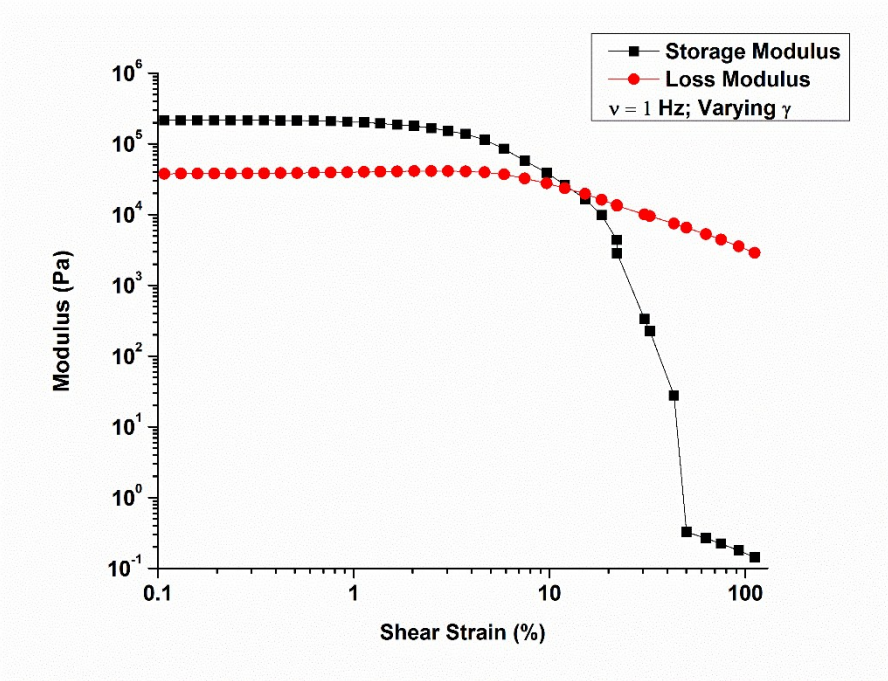

Figure S3. Oscillatory shear measurements (**strain sweep** - modulus vs. shear strain) for the optimized cerium-based gel.

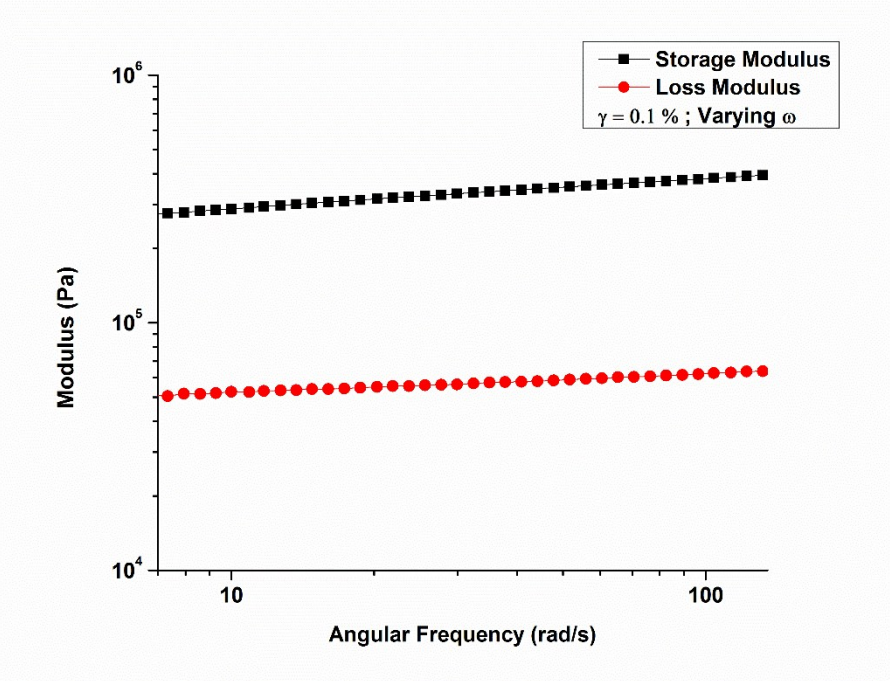

Figure S4. Oscillatory shear measurements (**frequency sweep** - modulus vs. frequency) for the optimized cerium-based gel.

The solid content of the various gels, cerium, ferric and aluminum-based, were estimated to be 4.99 %, 3.25 % and 1.99 %, respectively, by isothermal TGA at 100 ^{O}C. In comparison to the Chitosan-TPP (Tripolyphosphate) and Chitosan-PPi (Pyrophosphate) gels, they were lower in solid-content. The isothermal TGA thermograms for the various gels are presented in Figure S5.

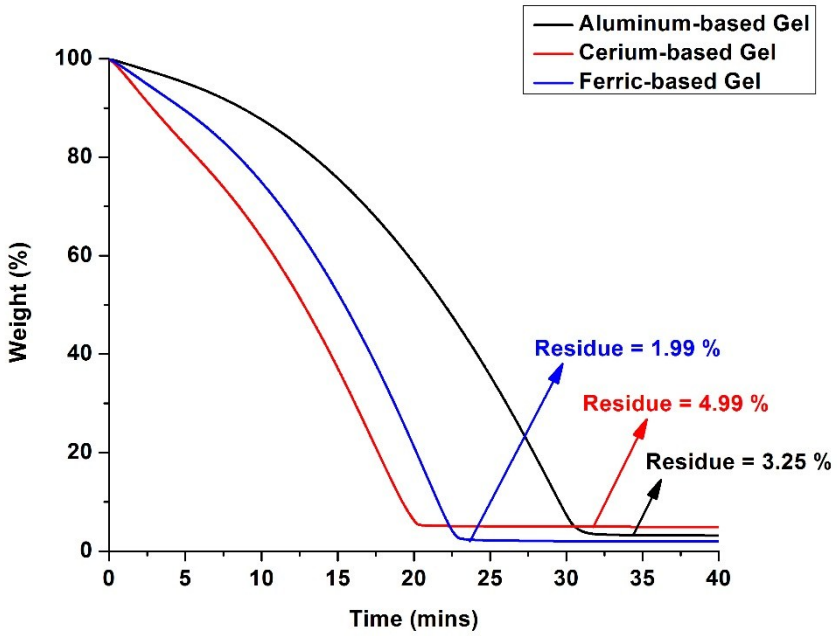

Figure S5. Isothermal TGA thermograms for the cerium, ferric and aluminum-based gels at 100 ^{O}C.

The strength of the various gels was compared using storage and loss moduli values, obtained through oscillatory shear rheological measurements. Among the gels, those based on cerium, yttrium, gadolinium and nickel, showed the highest storage moduli, while ferric, vanadium and other lanthanide-based gels gave an intermediate strength. Those based on aluminum and chromium, gave the poorest properties, however. Also, in all of the gels, the storage modulus dominated the loss modulus by almost an order of the magnitude, suggesting the viscoelastic behaviour. The similar loss factor also suggests that the mechanism of dissipation of energy is similar for all the gels. The comparison of storage and moduli of various gel systems are presented in Figure S6, while the loss factors of the same are presented in Figure S7.

The shear stability of the gels was determined from the oscillatory shear rheological measurements, at the cross-over point of G' and G''. Interestingly, the gels based on transition metal ions, in general, gave very good shear stability. Notably, the chromium-based gel gave a shear stability, in excess of 350 %, although its modulus was very low. On the other hand, gels based on lanthanides, gave an intermediate shear strength. Those based on cerium and yttrium, although highest in strength, gave very low shear stability. The comparison of the shear stabilities of various gels are presented in Figure S8.

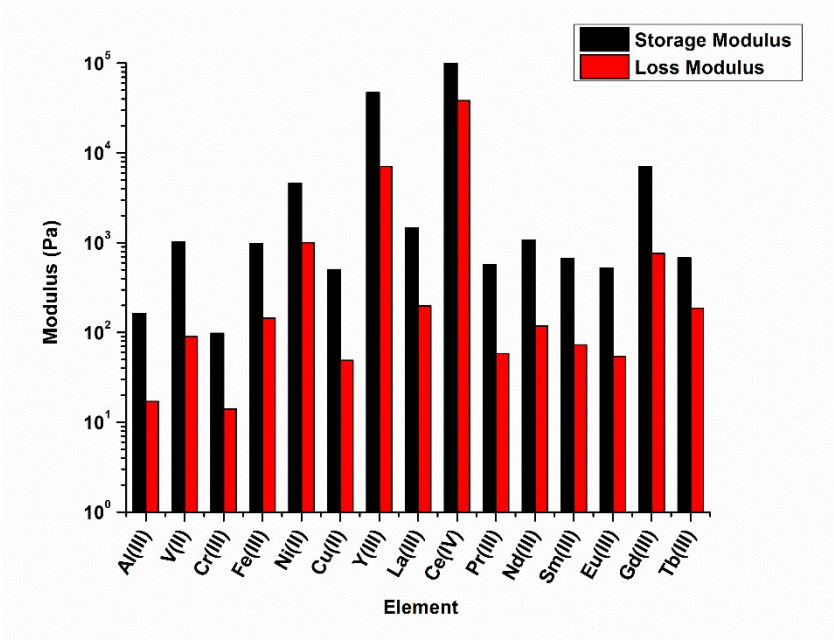

Figure S6. Comparison of storage and loss moduli of various gels.

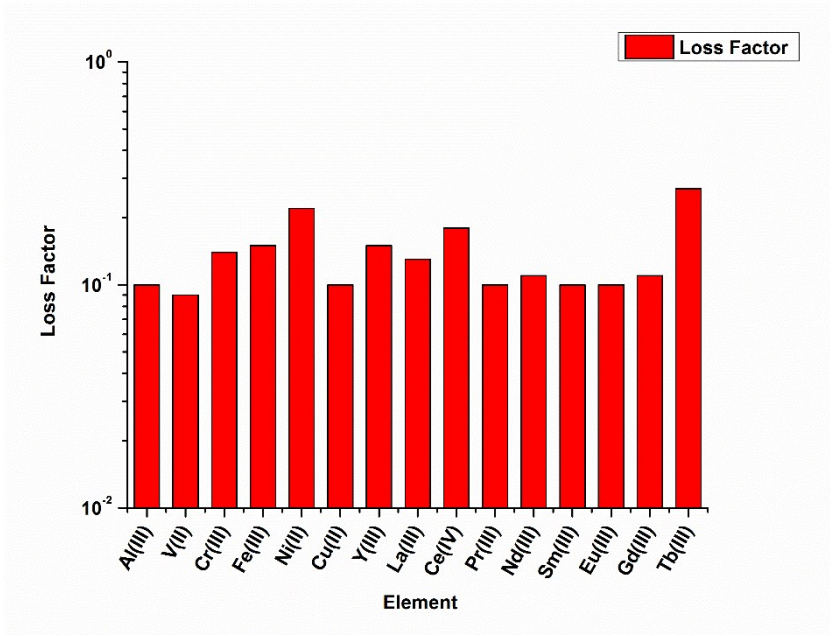

Figure S7. Comparison of loss factor of various gels.

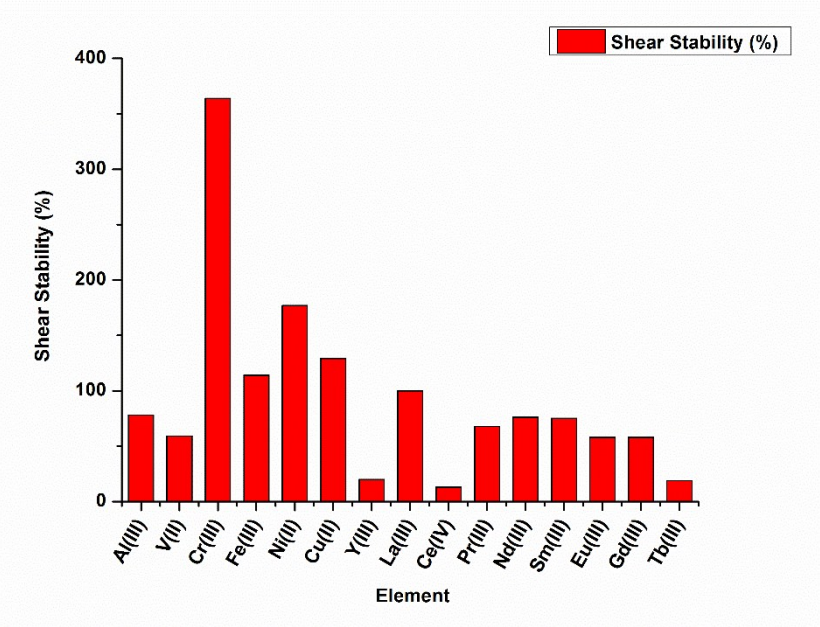

Figure S8. Comparison of shear stability (%) of various gels.

The gel-time, defined at the cross-over of G'' and G', was also determined using oscillatory shear rheological measurements. Raw chitosan showed no gelation under oscillatory shear, evident by the absence of any cross-over between G' and G''. As the molar ratio of $(NH_4)_2HPO_4$ was increased in the gel composition, with respect to chitosan, the gel-time was reduced. On the other hand, increase in CAN, increased the gel-time. Greater reaction rate, brought about by the increased concentration of $(NH_4)_2HPO_4$ with respect to CAN, is likely to be the cause. The gel-time for the various molar ratios of CAN and $(NH_4)_2HPO_4$ are given in Table S2, while the time sweeps for chitosan and various gels are given in the Figures S9, S10, S11, S12, S13 and S14 respectively.

Table S2. Gel-Time for Various Molar Ratios of the Cerium-based Gel.

Gel Composition (Chitosan: CAN: (NH4)2HPO4)	Gel Time (s)
1:0.3:0.5	176
1:0.3:1	41
1:0.3:1.5	38
1:0.1:1	18
1:0.5:1	61

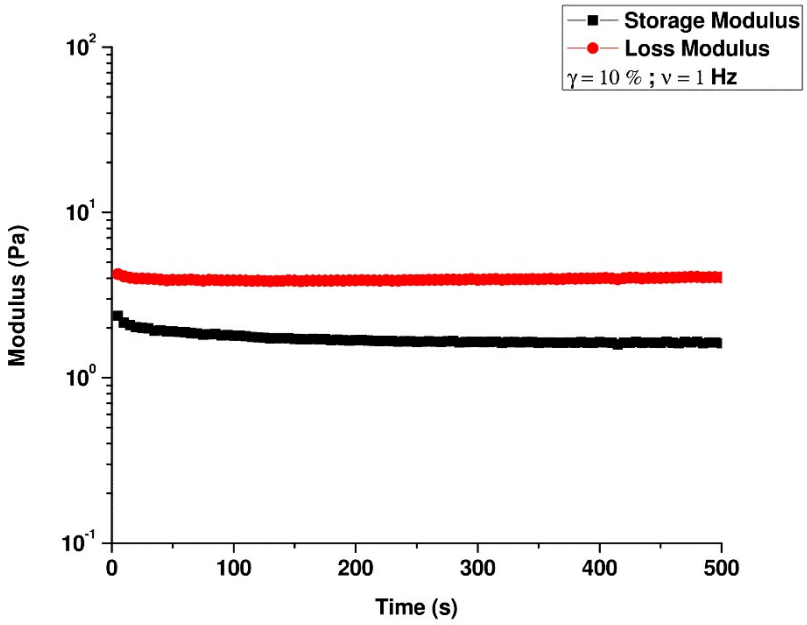

Figure S9. Oscillatory shear measurements (**time sweep** – modulus vs. shear strain) for chitosan solution (2. 5 w/v %).

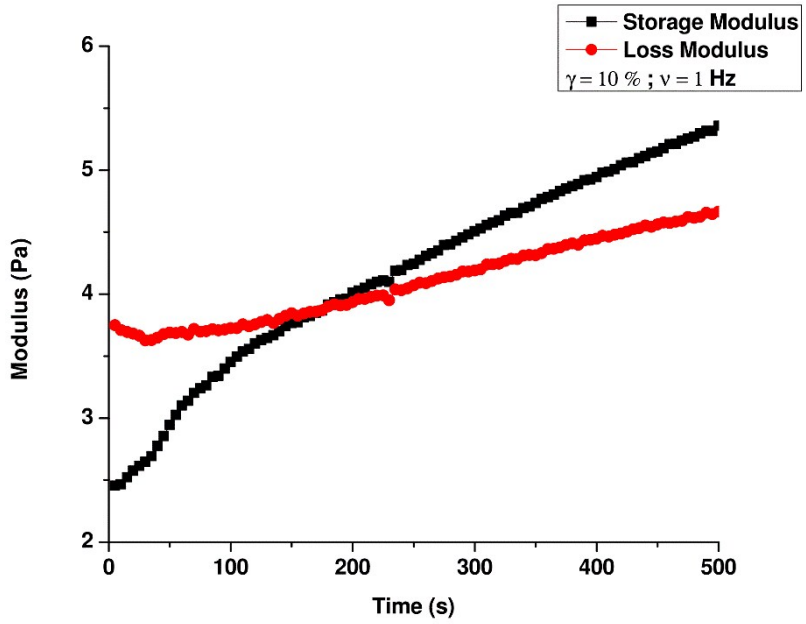

Figure S10. Oscillatory shear measurements (**time sweep** – modulus vs. shear strain) for the cerium-based gel (**chitosan: CAN: $(NH_4)_2HPO_4$ – 1: 0.3: 0.5**).

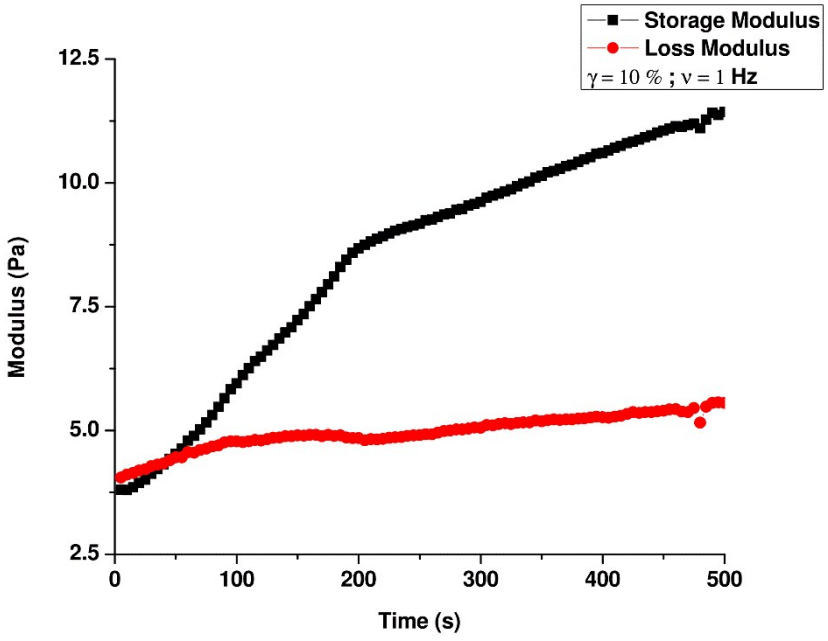

Figure S11. Oscillatory shear measurements (**time sweep** – modulus vs. shear strain) for the cerium-based gel (**chitosan: CAN: $(NH_4)_2HPO_4$ – 1: 0.3: 1**).

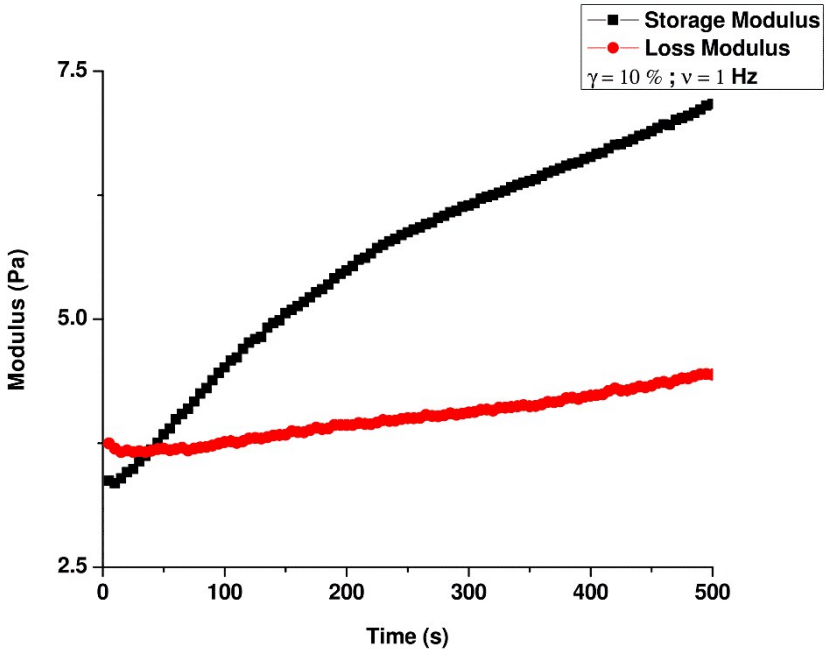

Figure S12. Oscillatory shear measurements (**time sweep** – modulus vs. shear strain) for the cerium-based gel (**chitosan: CAN: $(NH_4)_2HPO_4$ – 1: 0.3: 1.5**).

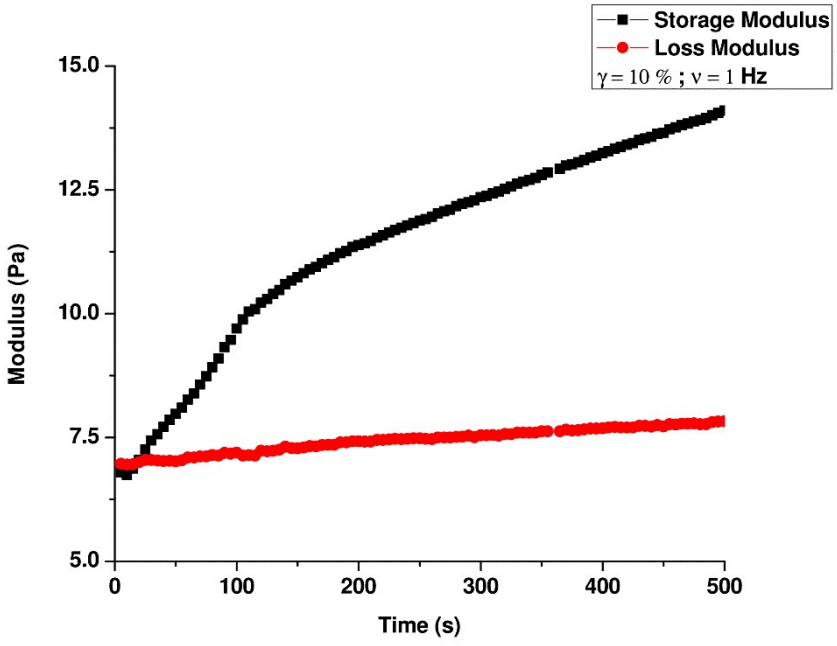

Figure S13. Oscillatory shear measurements (**time sweep** – modulus vs. shear strain) for the cerium-based gel (**chitosan: CAN: $(NH_4)_2HPO_4$– 1: 0.1: 1**).

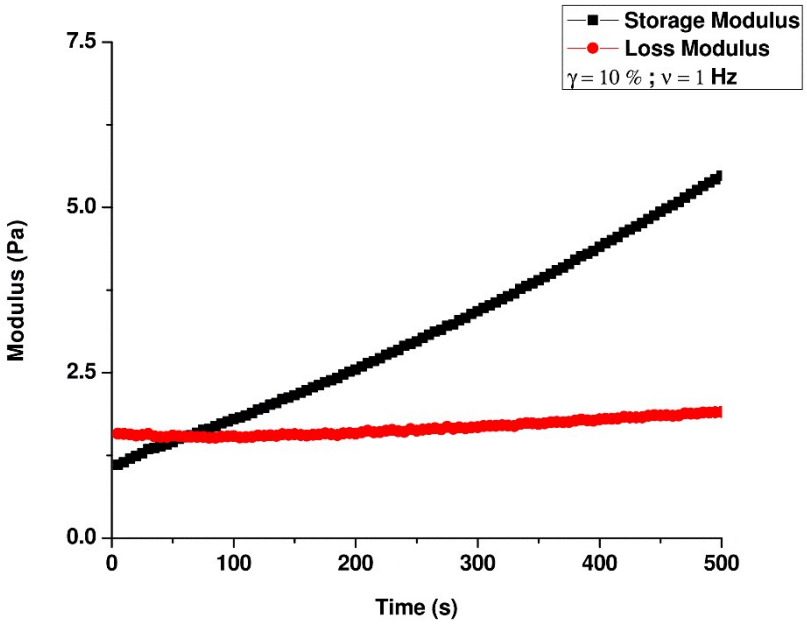

Figure S14. Oscillatory shear measurements (**time sweep** – modulus vs. shear strain) for the cerium-based gel **(chitosan: CAN: $(NH_4)_2HPO_4$ – 1: 0.5: 1).**

Chemical Analyses

The model gels, those-based on cerium and aluminum, were analysed using ^{31}P, ^{13}C, ^{27}Al solid state NMR, XRD and TGA. Figure S15 shows the ^{31}P solid state NMR spectrum for the external reference used: methyl triphenyl phosphonium iodide ($MePPh_3I$). Compared to the reported chemical shift of approximately 22 ppm in solution,[3–5] the standard gave three peaks at 29.33, 28.17, 25.75 ppm, respectively, in the solid state. Since, the NMR spectrometer was already calibrated with bromine signal for various nuclei, the shifts were assumed to be arising out of interactions in the solid state. The calibration of the other spectra was done-based on the standard peaks at 29.33, 28.17 and 25.75 ppm.

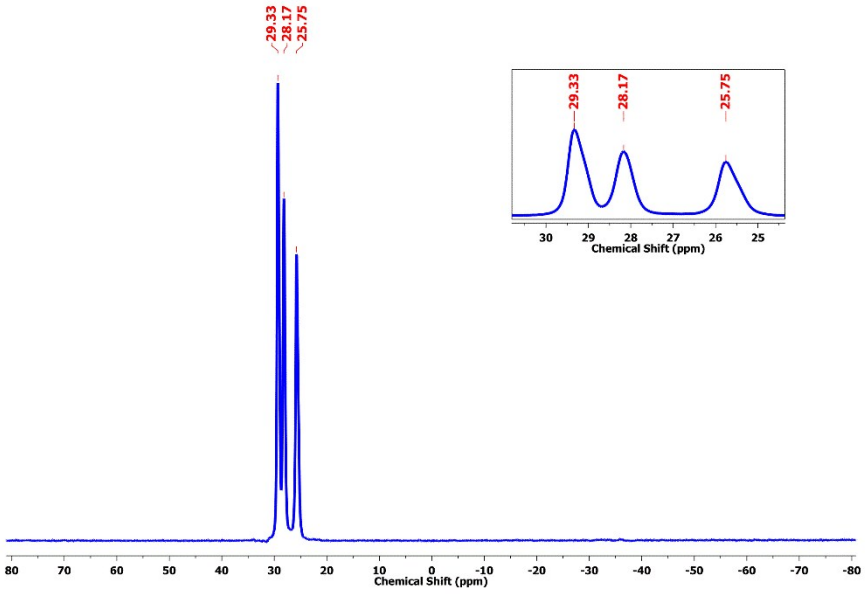

Figure S15. ^{31}P NMR spectrum for triphenyl phosphine NMR standard Used.

The ^{31}P NMR spectra for the $(NH_4)_2HPO_4$, chitosan + $(NH_4)_2HPO_4$ blend, aluminum phosphate and aluminum-based gel are presented in Figures S16, S17, S18 and S19, respectively. $(NH_4)_2HPO_4$ gave a single peak at 6.18 ppm. Upon blending with chitosan, the peak did not show any shift, indicating that the environment of the phosphate ion is unmodified. Aluminum phosphate, on the other hand, showed a very broad peak centered at -10.18 ppm. This corresponds to the HPO_4^- ion.[6,7] The broadness also indicates the varied environments of the phosphate ion, in this amorphous material. In presence of chitosan, the peak at -10.18 ppm undergoes downfield shift to -0.94 ppm. This shift of the new peak clearly indicates the interaction between the aluminum phosphate and chitosan. It is likely that the phosphate species interacts electrostatically with the NH_3^+ groups in chitosan solution, leading to the such observed shifts.[8] Additionally, a peak from bound/unwashed $(NH_4)_2HPO_4$ is also visible. The observed shifts of the phosphate peak, upon gelation, rather than the appearance of a new peak, indicates that chitosan-colloid interaction dominates the bulk interactions in the colloids. This suggests that the colloidal particles are very small in size, when generated, *in situ*, in chitosan solution. As soon as a colloidal particle is precipitated, its surface charge may have caused chitosan to cap it spontaneously, preventing any further agglomeration/growth of the particle.

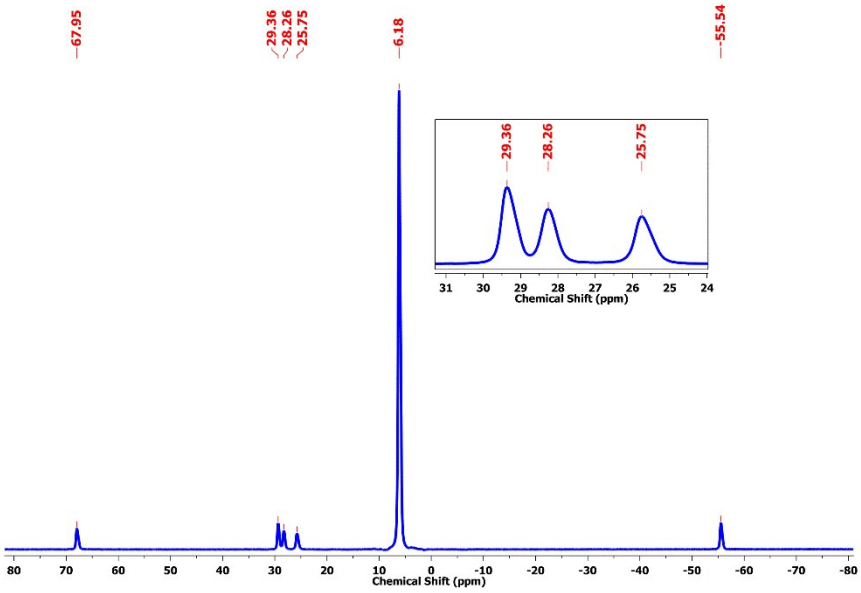

Figure S16. ^{31}P NMR spectrum for $(NH_4)_2HPO_4$.

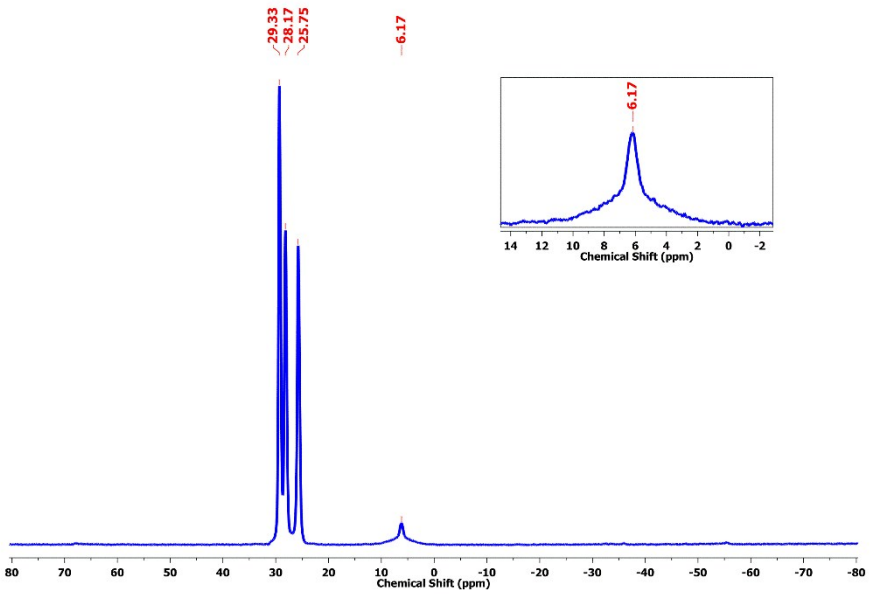

Figure S17. ^{31}P NMR spectrum for chitosan + $(NH_4)_2HPO_4$ product.

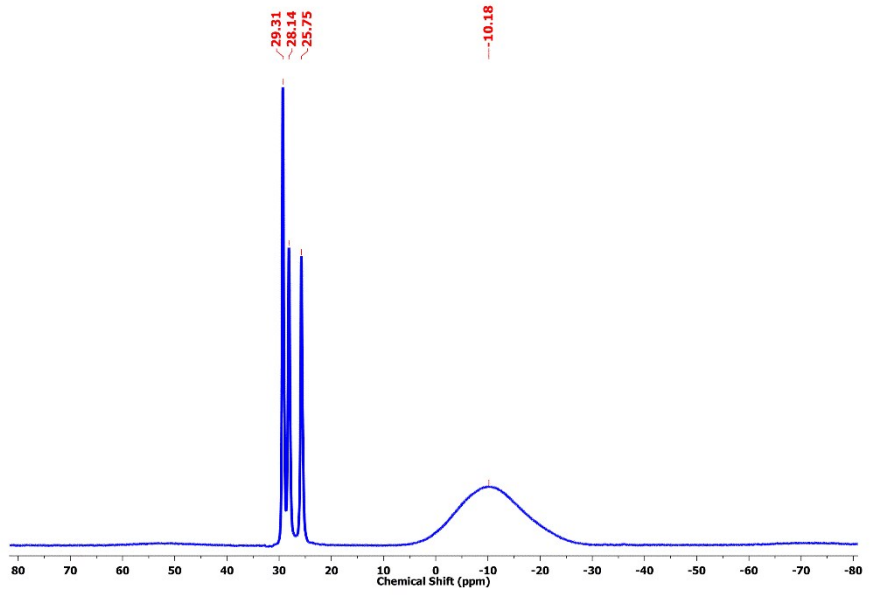

Figure S18. ^{31}P NMR spectrum for aluminum phosphate.

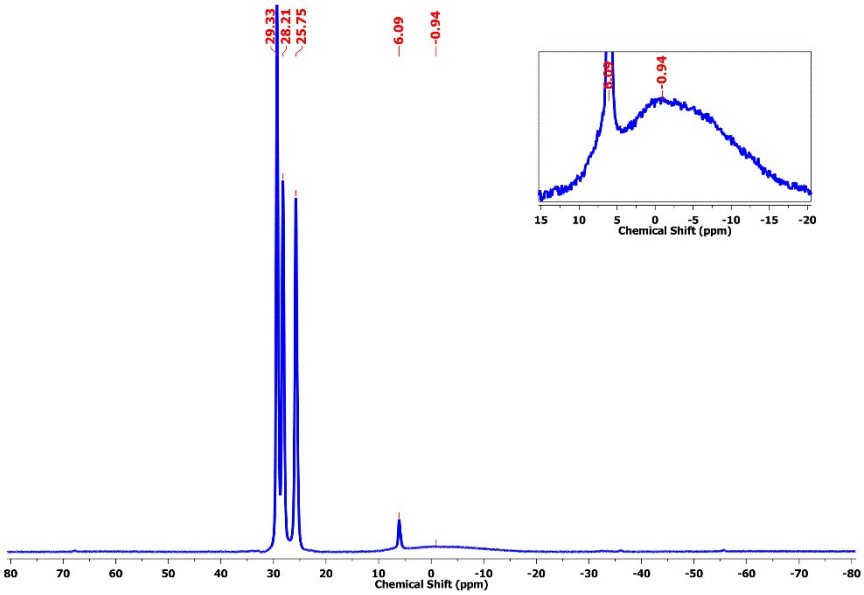

Figure S19. ^{31}P NMR spectrum for aluminum-based gel.

The ^{31}P NMR spectra for the cerium phosphate and cerium-based gel are presented in Figures S20 and S21, respectively. Cerium phosphate showed a very broad peak centered at -5.36 ppm. This corresponds to the $H_2PO_4^-$ ions.[6,7] The broadness also indicates the varied environments of the phosphate ion, in this amorphous material. In presence of chitosan, the peak at -5.36 ppm undergoes downfield shift to -3.58 ppm. This shift of the new peak clearly indicates the interaction between the cerium phosphate and chitosan. It is likely that the phosphate species interacts electrostatically with the NH_3^+ groups in chitosan solution, leading to the such observed shifts. Further, these shifts, rather than the appearance of a new peak, again indicate that the colloidal particles, generated *in situ*, are of very small sizes.

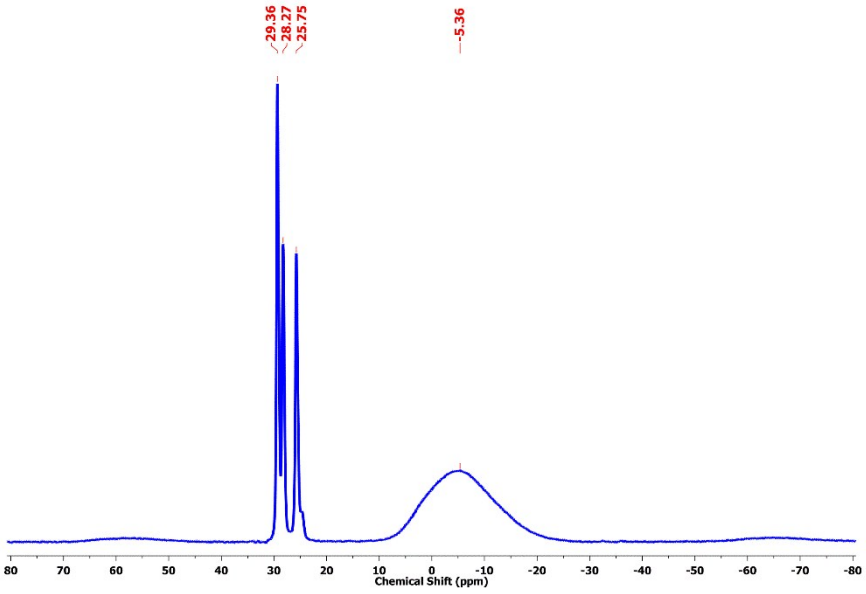

Figure S20. ^{31}P NMR spectrum for cerium phosphate.

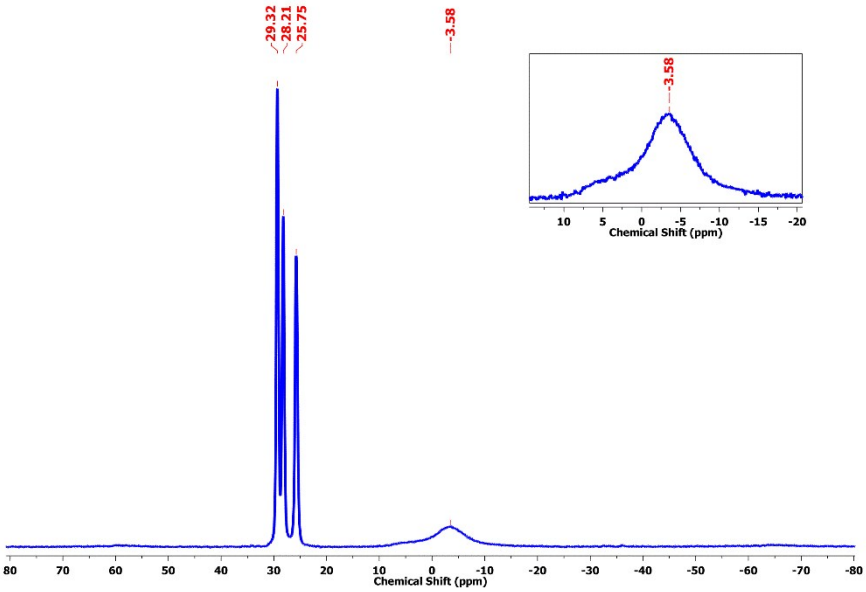

Figure S21. ^{31}P NMR spectrum for cerium-based gel.

Figure S22 shows the ^{13}C solid state NMR spectrum for Chitosan. The peaks are indexed as follows: 23.30 ppm (-CH_3), 57.38 ppm (C2), 61.03 ppm (C6), 75.03 ppm (C3, C5), 82.81 ppm (C4), 104.75 ppm (C1) and 174.13 ppm (C=O).[9]

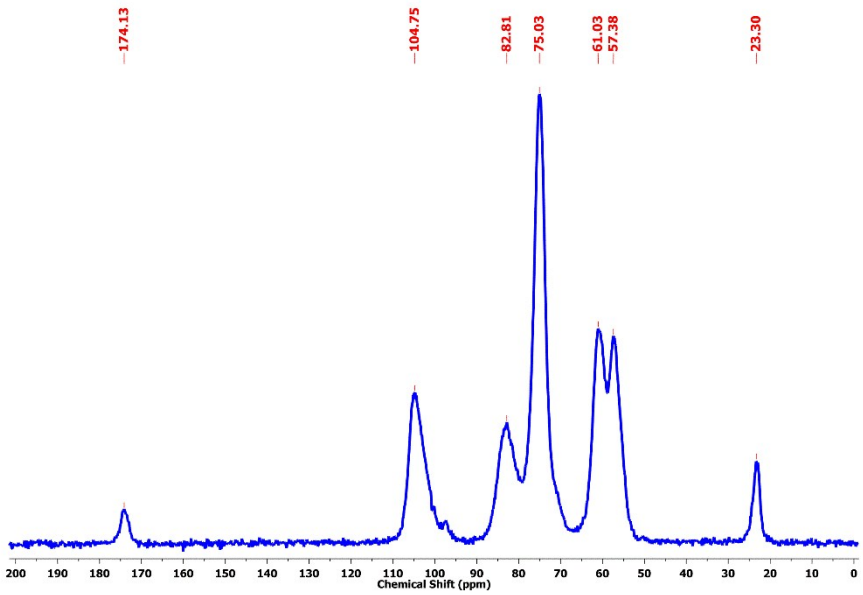

Figure S22. ^{13}C NMR spectrum for chitosan.

Upon gelation using CAN, however, the peaks corresponding to -CH_3 (23.3 ppm), C=O (173.46 ppm), C2 (56.99 ppm), C3 and C5 (74.86 ppm) were relatively unaffected, while those of C4 and C6 (59.78 ppm) showed significant upfield shifts, merging into the nearby peaks. The peak corresponding to C1 showed the most prominent upfield shift, from 104.75 to 96.89 ppm, whilst undergoing broadening. These shifts, most likely brought about by the interactions between chitosan and cerium phosphate and a subsequent loss in the inter- and intra-molecular H-bonding between the chitosan chains, confirm the changes in the environment of the chitosan upon gelation. The ^{13}C Solid State NMR spectrum for cerium-based gel is presented in Figure S23.

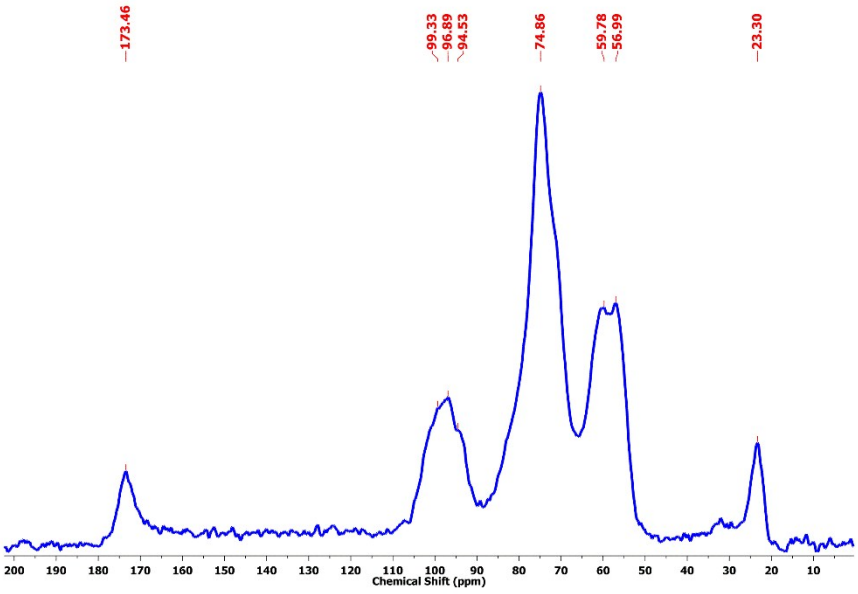

Figure S23. ^{13}C NMR spectrum for cerium-based gel.

Gelation using $AlCl_3$ produced remarkably similar shifts in the ^{13}C solid state NMR spectrum, as in the case of CAN. While, the peaks corresponding to $-CH_3$ (23.3 ppm), C=O (174.16 ppm), C2 (57.61 ppm), C3, C5 (74.79 ppm) were relatively unaffected, those of C4 and C6 showed significant upfield shifts, merging into the nearby peaks. The peak corresponding to C1 showed the most prominent upfield shift from 104.75 to 100.12 ppm, while broadening. These shifts result from interactions between chitosan and aluminum phosphate and a subsequent loss in the inter- and intra-molecular H-bonding between the chitosan chains, brought about by gelation. The ^{13}C solid state NMR spectrum for aluminum-based gel is presented in Figure S24.

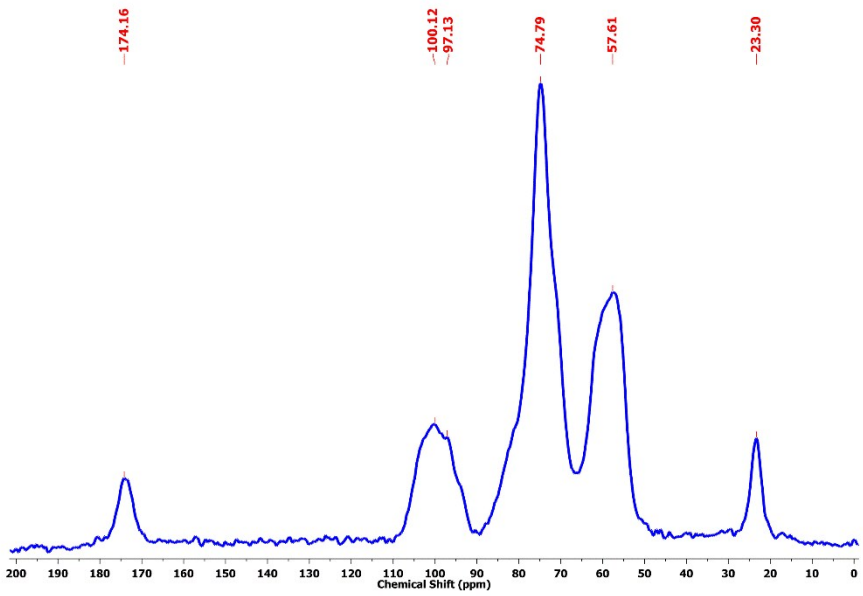

Figure S24. ^{13}C NMR spectrum for aluminum-based gel.

Surprisingly, chitosan + $(NH_4)_2HPO_4$ blend, prepared by the addition of $(NH_4)_2HPO_4$ to chitosan solution, followed by precipitation in methanol and drying, gave very similar shifts in the ^{13}C solid state NMR spectrum. Only the peaks corresponding to C4, C6 and C1 showed upfield shifts, while the remainder of the spectrum was unaffected. These shifts probably arise out of interactions between the chitosan and the phosphate ions. The presence of such shifts in the spectra of the gels (Figures S24 and S25) confirms the presence of interactions of similar nature in them. These chemical shifts suggest that the phosphate group might be located between the C1, C4 and C6 carbons, whilst electrostatically bonding to $-NH_3^+$ group at C2. The ^{13}C solid state NMR spectrum for chitosan + $(NH_4)_2HPO_4$ blend is presented in Figure S25.

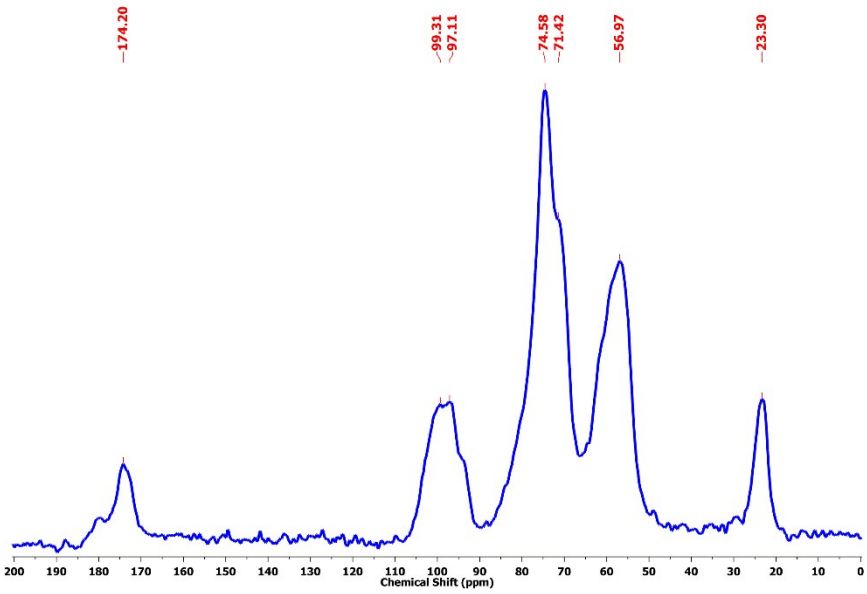

Figure S25. ^{13}C NMR spectrum for chitosan + $(NH_4)_2HPO_4$ blend.

The zeta potential values for various *ex situ* prepared metal phosphates are given in Table S3.

Table S3. Zeta potential values (mV) for various *ex situ* prepared metal phosphates.

Metal Phosphate	Zeta Potential (mV)
Fe (II)	0.0107
Mg (II)	-2.68
Ca (II)	-3.69
La (III)	-15
Cu (II)	-19.7
Al (III)	-29.3
Fe (III)	-33.4
Ce (IV)	-38.3

^{27}Al CP-MAS NMR spectrum for aluminum phosphate was performed to study the chemical environment of Al nuclei in the phosphate and the gel form. Interestingly both the phosphate and the gel, showed a similar NMR spectrum, indicating the non-participation of the metal cation in the gelation process. The peak at around 0 ppm corresponds to the octahedrally co-ordinated form of aluminum phosphate, while the other peak at around 50 ppm corresponds to the tetrahedrally co-ordinated form.[10–12] ^{27}Al CP-MAS NMR spectra for the aluminum phosphate and the optimized gel are presented in Figures S26 and S27, respectively.

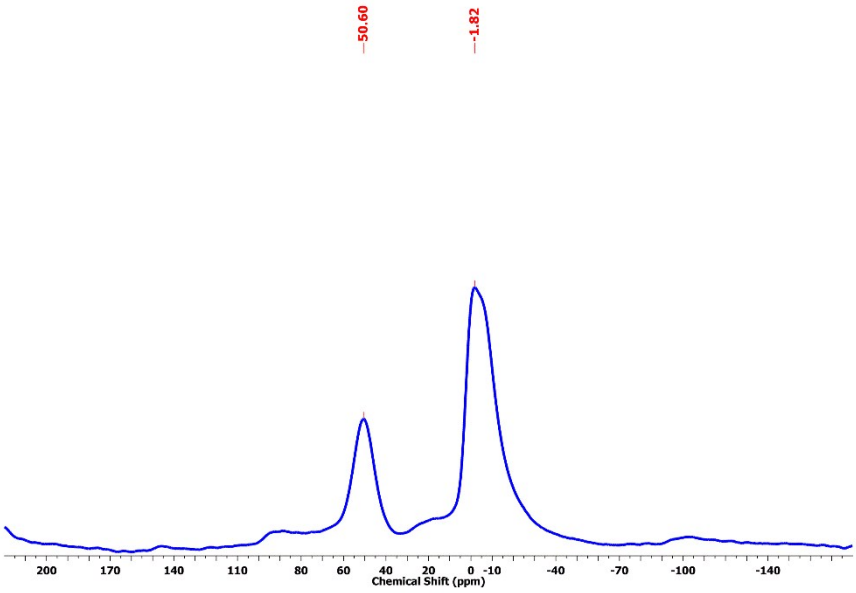

Figure S26. ^{27}Al NMR spectrum for aluminum phosphate.

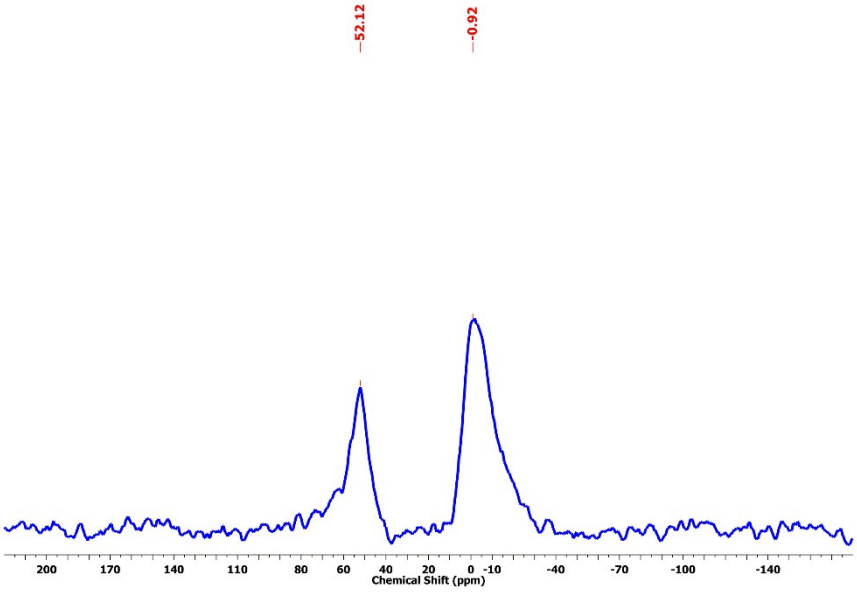

Figure S27. ^{27}Al NMR spectrum for aluminum-based gel.

In order to confirm that gelation does not occur by precipitation of chitosan, pH metric study was performed, which is presented in Figures S28 and S29. From these figures, it is clear that the pH of chitosan solution does not change significantly upon addition of $(NH_4)_2HPO_4$ or metal salt (Here, Fe $(NO_3)_3$). Likewise, the order of addition of the two precursors also caused no significant changes in pH. In all the cases, the final pH was below 4, which is much below the critical pH of ~6 for chitosan dissolution[13]. Another "proof" of the mechanism lies in a control experiment involving H_3PO_4. Choice of H_3PO_4 in place of $(NH_4)_2HPO_4$ also resulted in gelation. This means that the gelation occurs truly due to the colloidal phosphates, generated *in situ*.

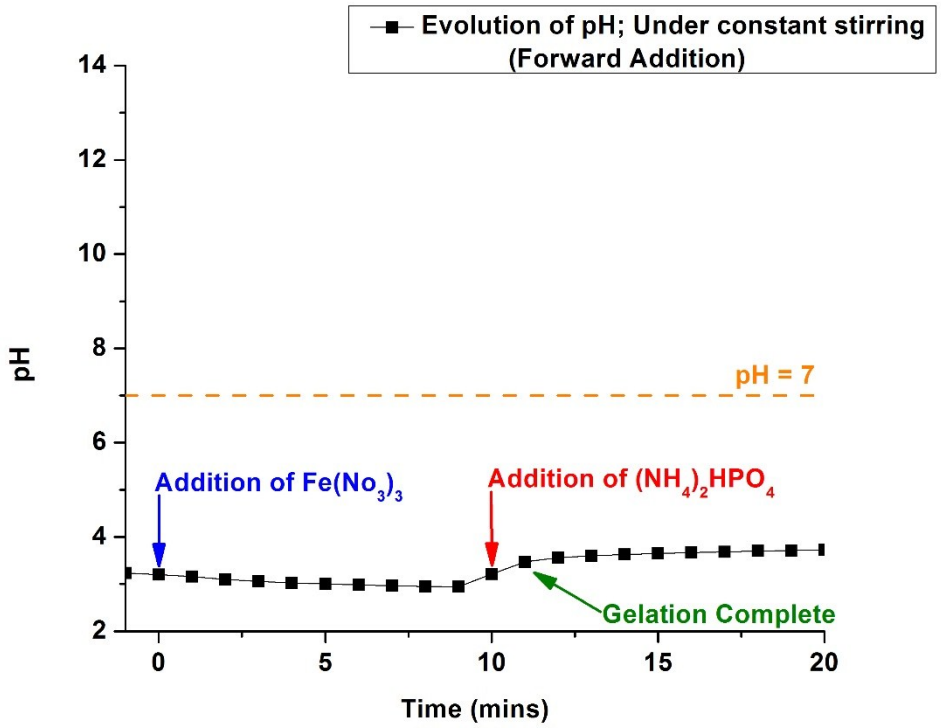

Figure S28. Evolution of pH, during the various stages of gelation (forward addition).

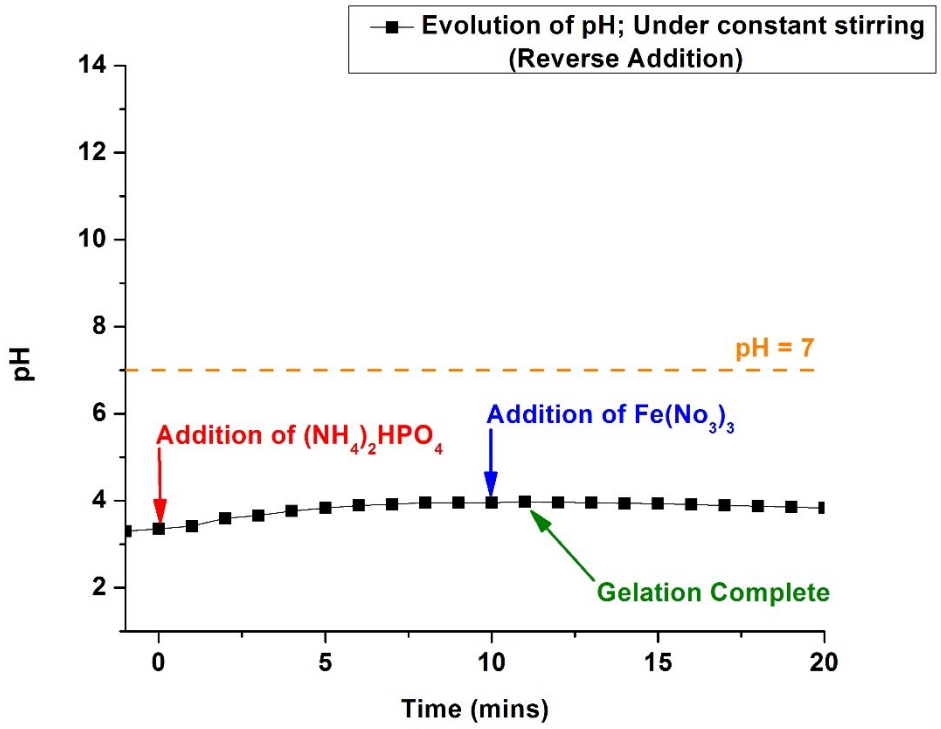

Figure S29. Evolution of pH, during the various stages of gelation (reverse addition).

The WAXS profiles for the chitosan, cerium phosphate, cerium-based gel and chitosan + $(NH_4)_2HPO_4$ blend are given in Figure S30. Chitosan showed a semi-crystalline nature. The two peaks at 9.3^O and 20^O correspond to the 020 and 110 planes of the chitosan crystal. Unlike chitosan, its blend with $(NH_4)_2HPO_4$, showed a complete loss in the crystallinity, evident by a large amorphous peak at 23.1^O. The peak at 9.3^O and 20^O, shifted to 11.7^O and 18.5^O, respectively, whilst broadening and reducing in its intensity drastically. No peaks corresponding to $(NH_4)_2HPO_4$ were observed. Cerium phosphate, on the other hand, showed an amorphous nature, evident by the broad amorphous peaks. Likewise, upon gelation, a completely amorphous phase had resulted. This was due to extensive crosslinking of the chitosan chains, which prevented recrystallization upon removal of water from the synthesized gel.

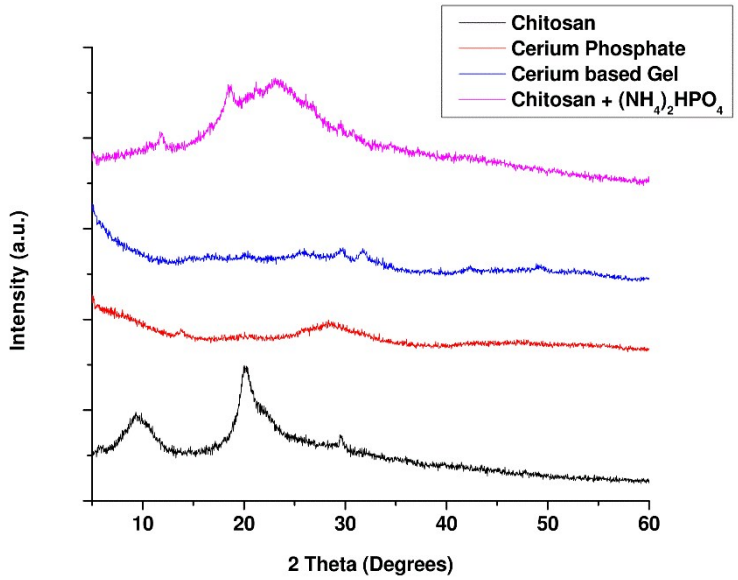

Figure S30. WAXS profiles for chitosan, cerium phosphate, CAN-based gel and chitosan + $(NH_4)_2HPO_4$ blend.

The XRD patterns for the chitosan, aluminum phosphate, aluminum-based gel and chitosan + $(NH_4)_2HPO_4$ are given in Figure S31. Aluminum phosphate showed an amorphous nature, evident by the broad amorphous peaks, with few low-intensity sharp peaks, centered around 16.8^O, 20.6^O, 23.9^O and 29.2^O. Upon gelation, a completely amorphous material had resulted due to crosslinking of the chitosan chains which prevented subsequent recrystallization.

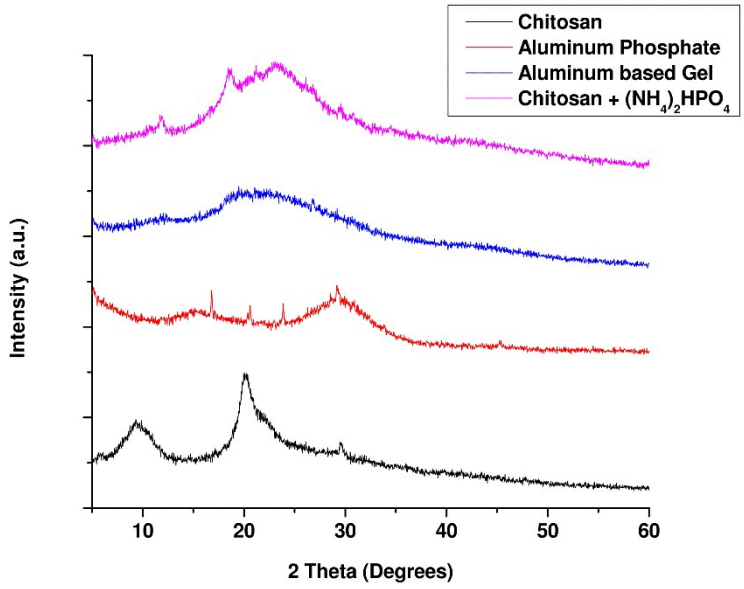

Figure S31. WAXS profiles for chitosan, aluminum phosphate, aluminum-based gel and chitosan + $(NH_4)_2HPO_4$ blend.

Thermogravimetry was also performed on chitosan, cerium phosphate, cerium-based gel and chitosan + $(NH_4)_2HPO_4$ blend. Chitosan showed a one stage degradation process, with the onset decomposition temperature ($T_{D, Onset}$) at 208 ^{O}C and peak decomposition temperature ($T_{D, Peak}$) at 299 ^{O}C. On the other hand, cerium phosphate showed a three-stage degradation process. The first step ($T_{D, Peak}$ = 72 ^{O}C) between 43 ^{O}C and 142.4 ^{O}C corresponded to the loss of water molecules outside the hydration sphere, while the second step ($T_{D, Peak}$ = 264 ^{O}C) arises from both the loss of water molecules within the hydration sphere and the dehydroxylation of the phosphate anions. The third broad, overlapping step, beyond 342 ^{O}C, corresponds solely to the dehydroxylation of the remainder phosphate anions, leading to the formation of pyrophosphates. The weight loss during the second step was observed to be 16.90 %, which accounts for 5.75 water molecules; 4.75 of those, probably arising from dehydration of crystallized water molecules and 1 water molecule, from the dehydroxylation of $(H_2PO_4)^-$. The third step, having a weight loss of 8.77 %, accounts for the remainder of the 3 water molecules from the dehydroxylation process. Hence, the approximate molecular formula was predicted to be $Ce(H_2PO_4)_4$. $4.75H_2O$. Formation of colloidal salt of $(H_2PO_4)^-$, rather than that of $(HPO_4)^{2-}$, is further confirmed from chemical shifts, observed with ^{31}P NMR spectroscopy.

Chitosan blended with $(NH_4)_2HPO_4$, showed a two-step degradation process. The first step ($T_{D, Peak}$ = 75 ^{O}C) corresponds to the loss of loosely bound moisture and ammonia from the $(NH_4)_2HPO_4$ salt. The second ($T_{D, Peak}$ = 234 ^{O}C) derivative peak corresponds to degradation of chitosan. Two shoulders around 300 ^{O}C and 500 ^{O}C appear, which are due to the dehydroxylation of the $(HPO_4)^{2-}$ anion. The decrease in the T_D of chitosan, observed in the TGA, can also be correlated with the XRD measurements, which showed a loss in the crystallinity of chitosan. It is likely that $(NH_4)_2HPO_4$ interacts with chitosan, disrupting the crystallinity, leading to the observed decrease in the T_D. Likewise, upon gelation, a two-stage degradation was observed. The first derivative peak around 42 ^{O}C corresponds to the weight loss due to the loosely bound moisture, while the second derivative peak at 238 ^{O}C, arises from the degradation of chitosan. A shoulder around 320 ^{O}C, corresponding to the dehydroxylation of the metal phosphates is also visible. As expected, the lowered T_D can be correlated with the XRD, which shows complete amorphousization upon gelation. The TGA and Derivative Thermogram (DTG) for chitosan, cerium phosphate, cerium-based gel and chitosan + $(NH_4)_2HPO_4$ blend are presented in Figures S32 and S33, respectively.

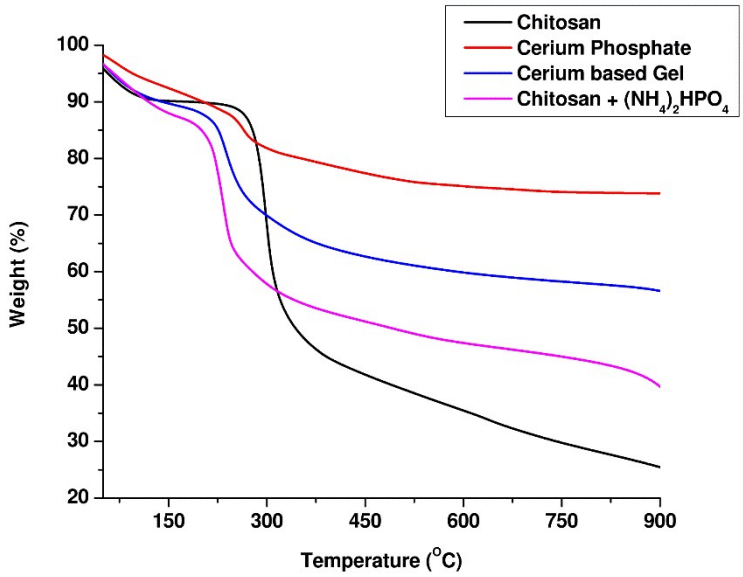

Figure S32. TGA thermograms for chitosan, cerium phosphate, cerium-based gel and chitosan + $(NH_4)_2HPO_4$ blend.

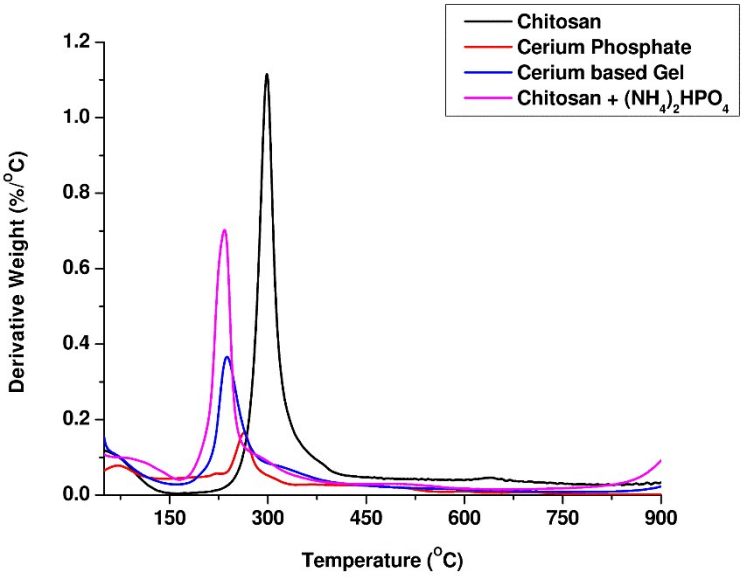

Figure S33. DTG thermograms for chitosan, cerium phosphate, cerium-based gel and chitosan + $(NH_4)_2HPO_4$ blend.

Thermogravimetry was performed on aluminum phosphate and aluminum-based gel. Aluminum phosphate showed a four-stage degradation process. The first step, below 45 ^{O}C corresponded to the loss of water molecules outside the hydration sphere. The broad, overlapping second ($T_{D,\ Peak}$ = 96 ^{O}C) and the third ($T_{D,\ Peak}$ = 231 ^{O}C) derivative peaks corresponds to loss of water molecules within the hydration sphere. The continuous weight loss beyond 300 ^{O}C up to 900 ^{O}C corresponds to the dehydroxylation of the phosphate anion, leading to the formation of $Al_2(PO_4)_3$. Due to the overlapping of the third and the fourth derivative peaks, individual contribution to the weight loss could not be measured. However, the combined weight loss accounted for 9.79 %, which roughly matched with the calculated value of 9.98 % for one crystallized water molecule and dehydroxylation of the $Al_2(HPO_4)_3$. The second derivative peak, again due to the crystallized water, corresponded to a weight loss of 18.16 %, accounting for approximately 4.4 units. Hence, the approximate molecular formula was predicted as $Al_2(HPO_4)_3$. $5.4H_2O$. Likewise, upon gelation, a two-stage degradation was observed. The first derivative peak around 75 ^{O}C corresponds to the weight loss due to the loosely bound moisture, while the second derivative peak at 240 ^{O}C, arises from the degradation of chitosan. A shoulder around 300 ^{O}C, corresponding to the dehydroxylation of the metal phosphates is also visible. As expected the lowered T_D can be correlated with the XRD, which shows complete amorphousization upon gelation. The TGA and DTG for the chitosan, aluminum phosphate, aluminum-based gel and chitosan + $(NH_4)_2HPO_4$ blend are presented in Figures S34 and S35, respectively.

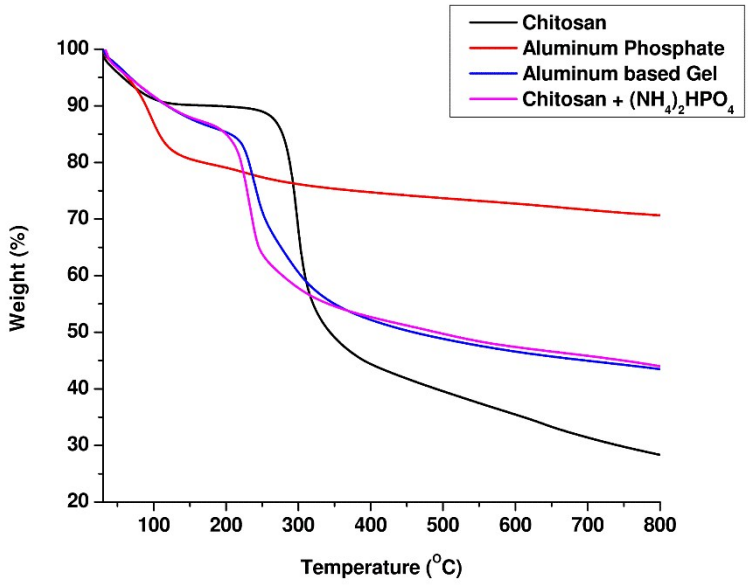

Figure S34. TGA thermograms for chitosan, aluminum phosphate, aluminum-based gel and chitosan + $(NH_4)_2HPO_4$ blend.

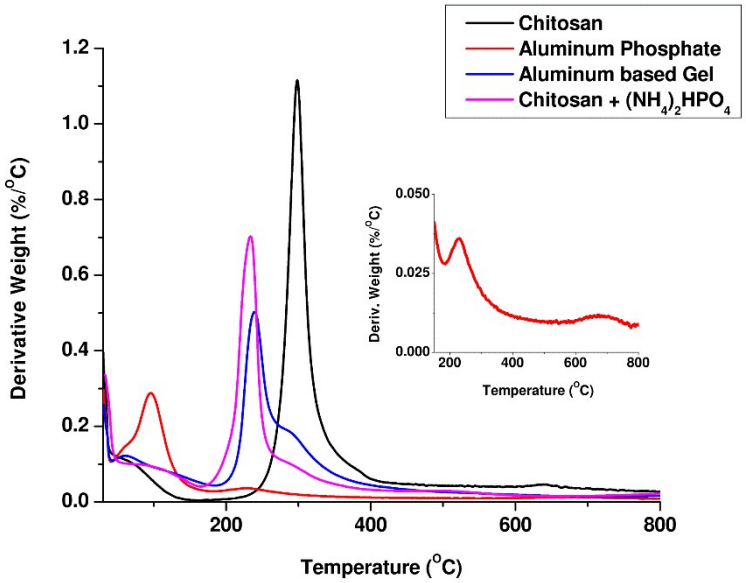

Figure S35. DTG thermograms for chitosan, aluminum phosphate, aluminum-based gel and chitosan + $(NH_4)_2HPO_4$ blend.

Colloids of cerium and ferric phosphate gave a morphology comprising of highly connected, quasi-spherical beads. Surprisingly, in the case of cerium, these beads had self-assembled into wires. On the other hand, colloidal aluminum phosphate gave particles of completely irregular shape and size. Few SEM micrographs are presented in figure S36, S37 and S38.

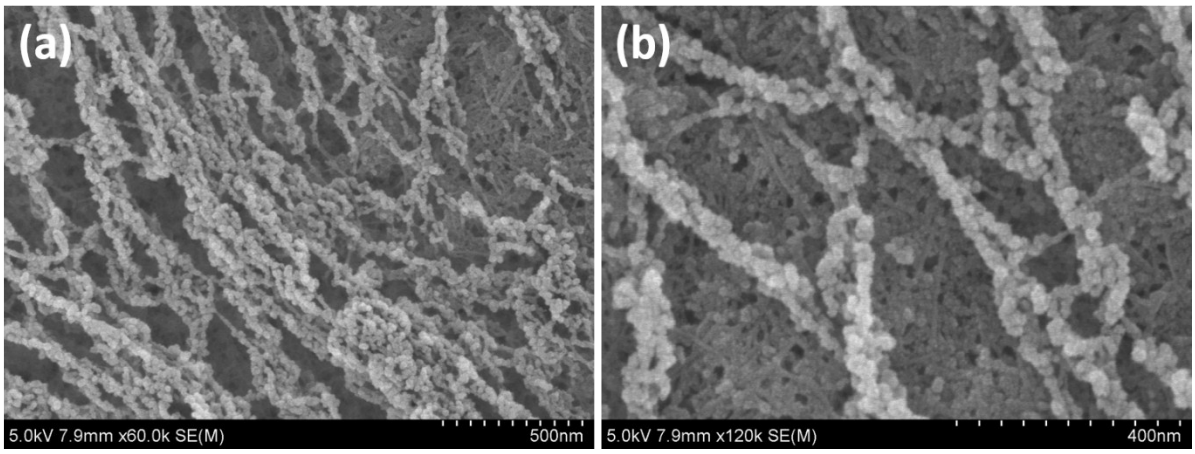

Figure S36. SEM micrographs of colloidal cerium phosphate.

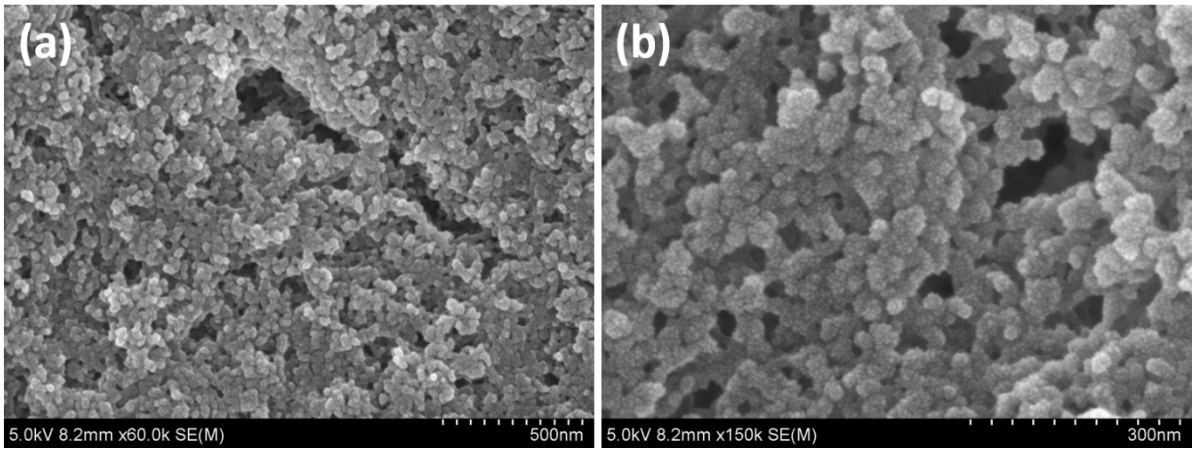

Figure S37. SEM micrographs of colloidal ferric phosphate.

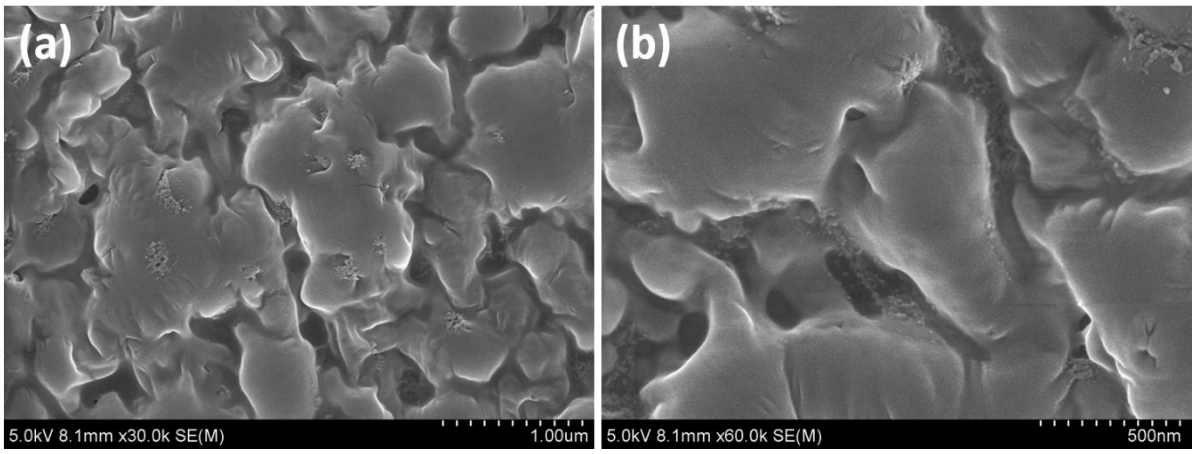

Figure S38. SEM micrographs of colloidal aluminum phosphate.

The *ex situ* prepared cerium, ferric and aluminum phosphates gave sizes of 255.1 ± 1.499 nm, 162.9 ± 88.9 nm and 808.2 ± 190.1 nm, respectively. The size distributions of the same, obtained using DLS measurements, are presented in Figures S39-S41. However, these sizes and distributions are not representative of *in situ* generated colloidal metal salts. Upon the formation of metal phosphates, *in situ*, in chitosan solution, the negative surface charge of the colloidal particles causes spontaneous coagulation. This should, in theory, produce very fine colloidal dispersions, when compared to *ex situ* prepared systems. This spontaneous coagulation, however, makes it very difficult to determine the size and the distribution of *in situ* generated colloidal particles.

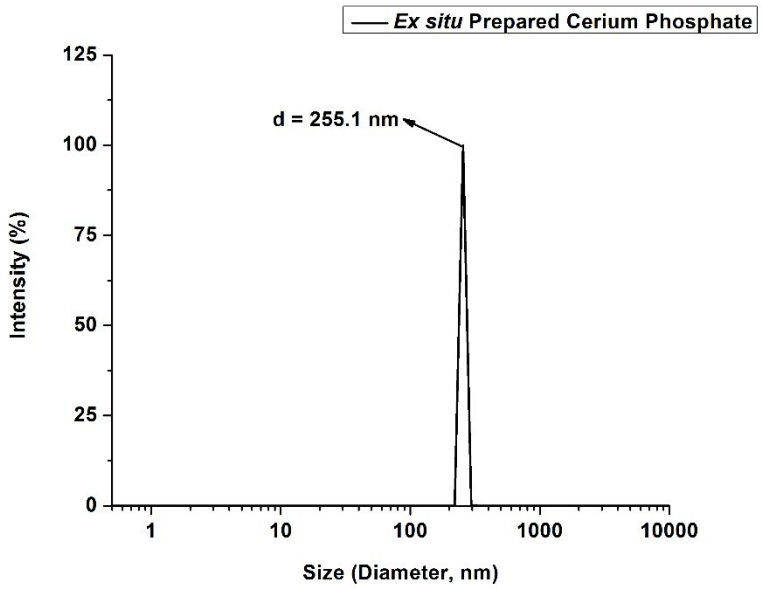

Figure S39. Size distribution of *ex situ* cerium phosphate colloids, obtained with DLS.

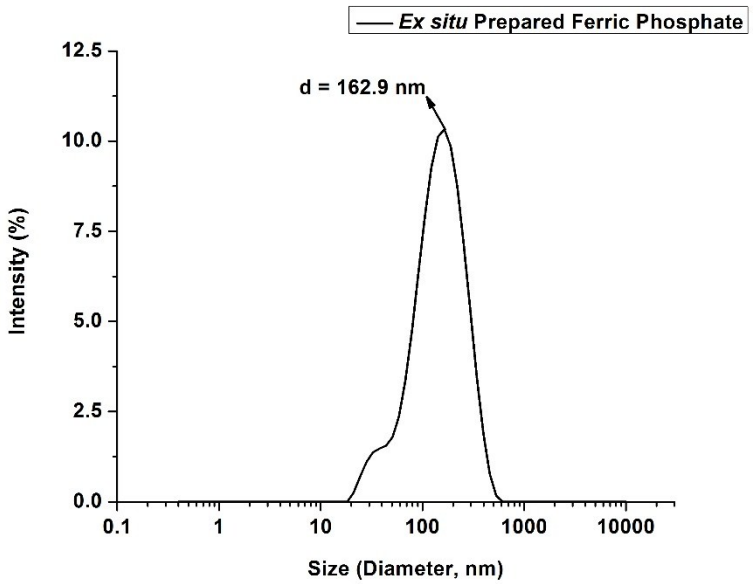

Figure S40. Size distribution of *ex situ* ferric phosphate colloids, obtained with DLS.

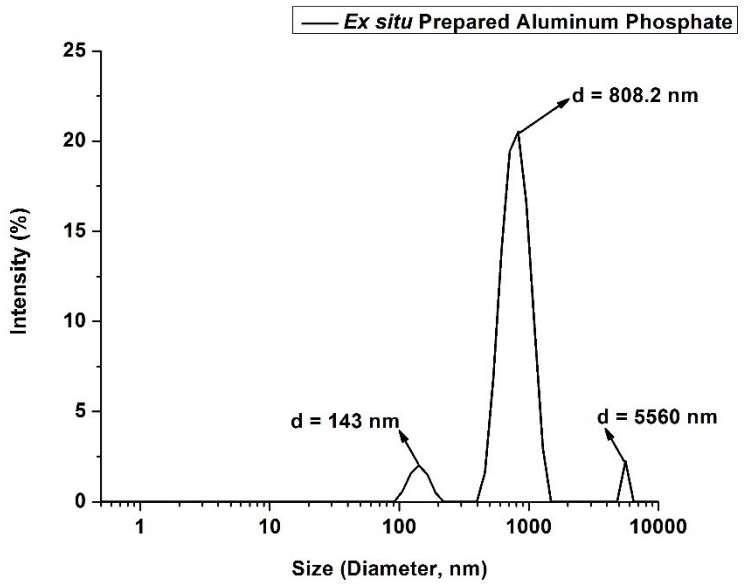

Figure S41. Size distribution of *ex situ* aluminum phosphate colloids, obtained with DLS.

Gel particles, prepared by *in situ* formation of colloidal salts in dilute low molar mass chitosan solution (concentration of 0.1 wt. %, rather than 2.5 wt. % solution which had been used throughout), were quasi-spherical in shape in all the cases. High resolution SEM and TEM micrographs showed that these gel particles had a completely smooth surface, free of any heterogeneity or undulations. This suggests that the colloidal particles are of very small sizes, much less than that of *ex situ* preparations. The homogeneity of the final gel was further confirmed by elemental mapping, whereupon all the elements were found to be homogeneously dispersed. The SEM micrographs of the gel particles are presented in Figures S42-44, while the EDS maps are presented in Figures S45-S46.

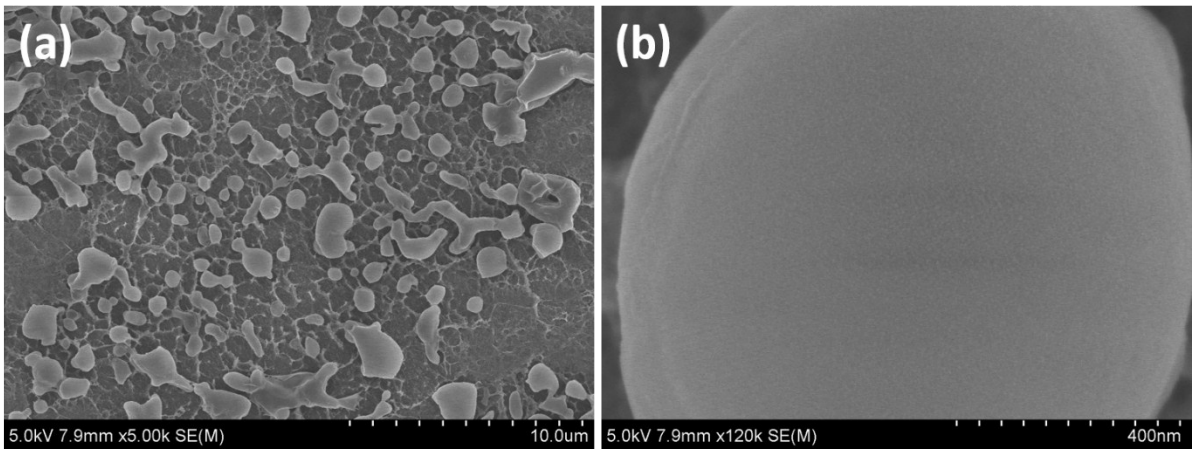

Figure S42. SEM micrographs of cerium gel particles.

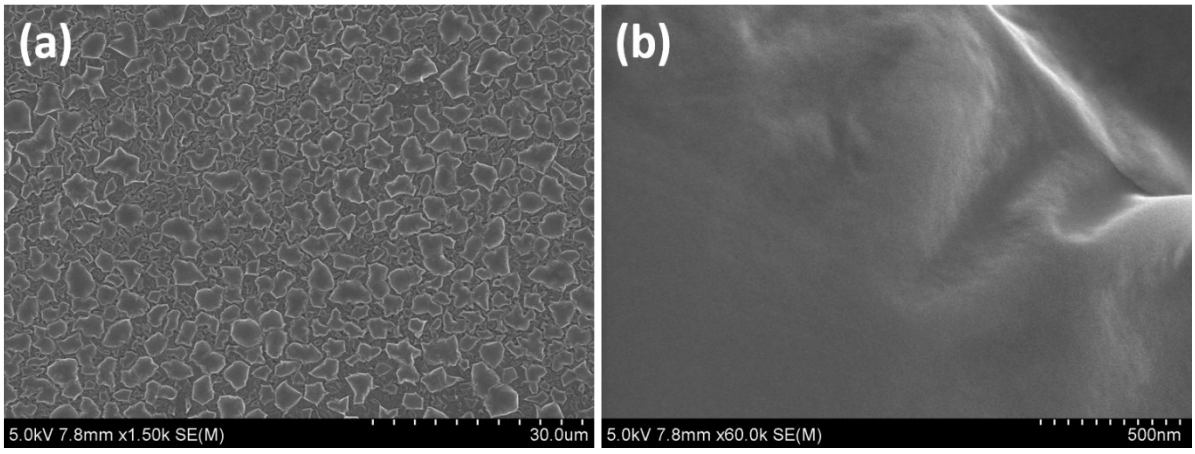

Figure S43. SEM micrographs of ferric gel particles.

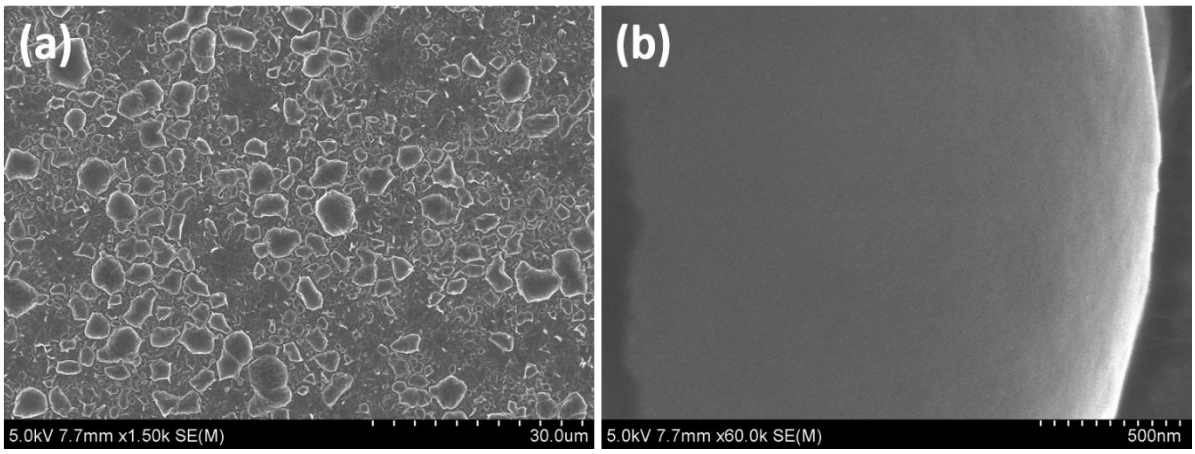

Figure S44. SEM micrographs of aluminum gel particles.

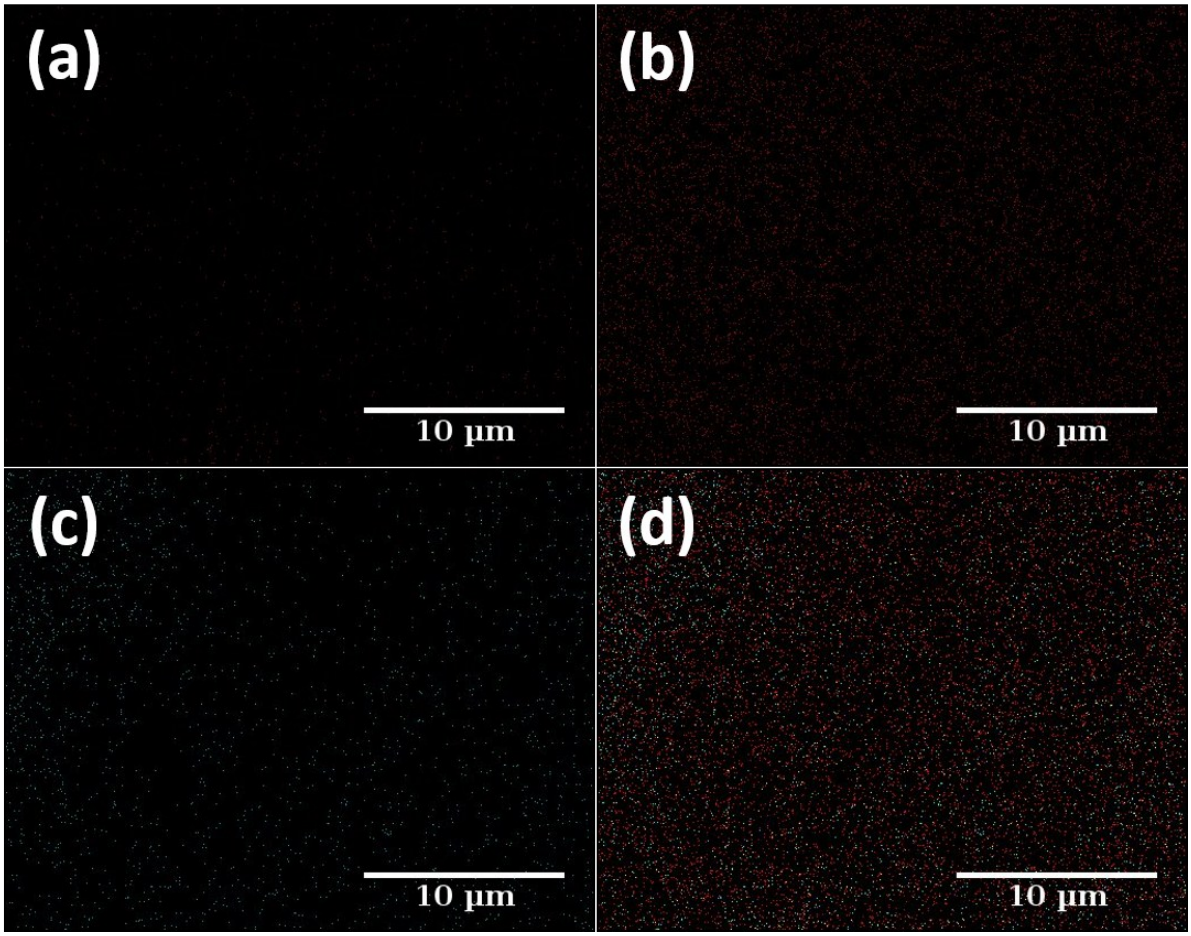

Figure S45. Elemental maps of (a) C (K shell) (b) Ce (L shell) (c) P (K shell) and (d) Overall [Ce (L Shell) •, N (K Shell) •, O (K Shell) •, C (K Shell) •, P (K Shell) •] in the cerium-based gel.

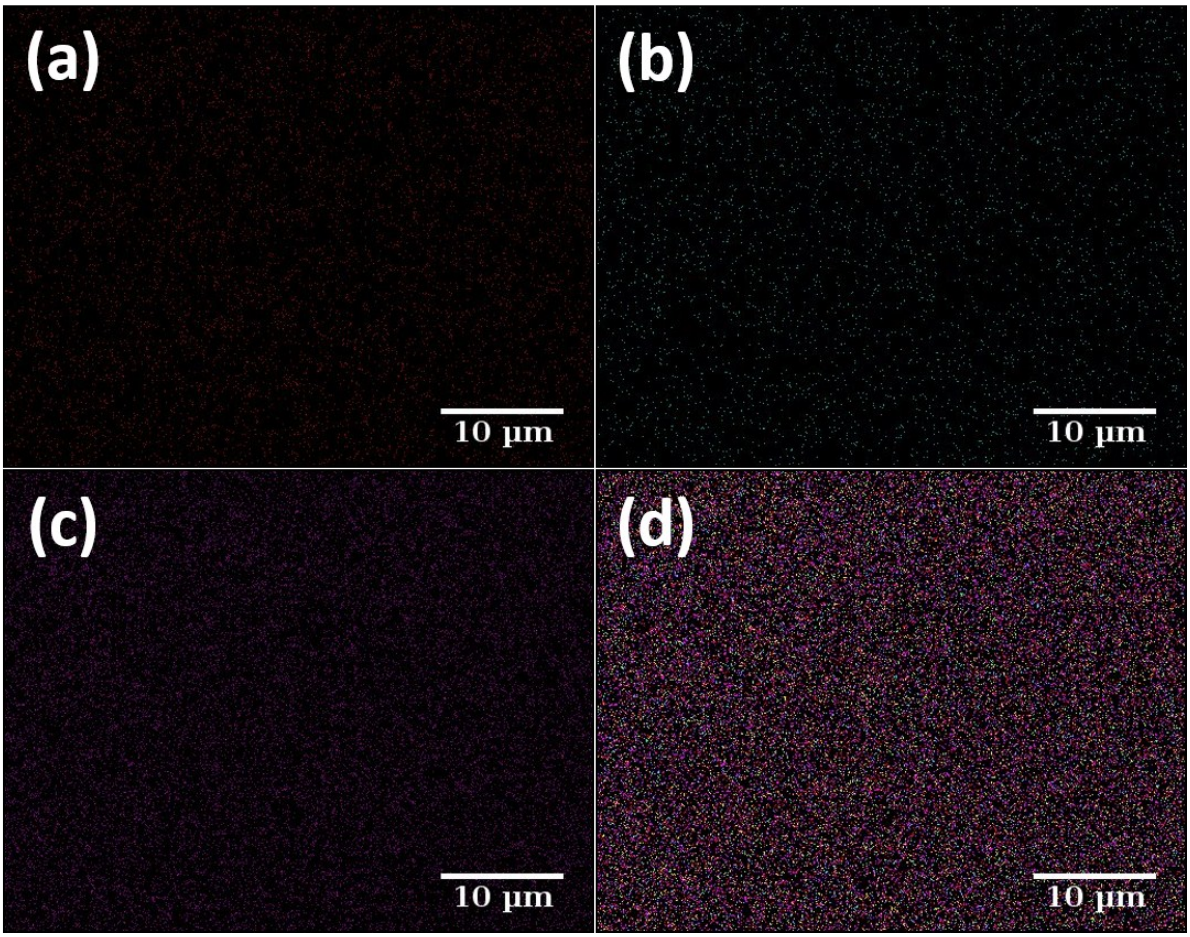

Figure S46. Elemental maps of (a) C (K shell) (b) Fe (K shell) (c) P (K shell) and (d) Overall [C (K Shell) •, N (K Shell) •, O (K Shell) •, Fe (K Shell) •, P (K Shell) •] in the ferric-based gel.

Upon freeze-drying, all the gels gave a layered structure. This was due to the formation of *Liesegang* bands, caused by the formation of a region of supersaturation first, rather than spontaneous precipitation, upon mixing of the two reagents. The *Liesegang* architecture and the SEM micrographs are presented in Figure S47. It may also be noted that these structures were also smooth and free of any heterogeneity or any undulations, when observed at high magnifications.

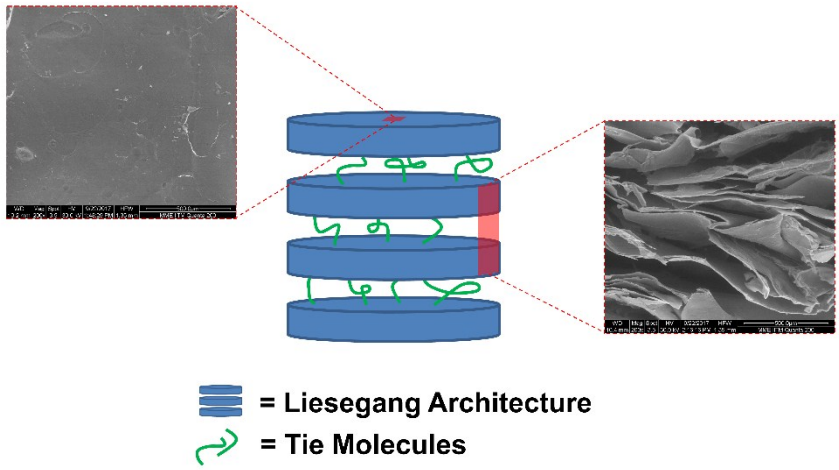

Figure S47. Pictorial representation of the *Liesegang* architecture observed for the cerium-based gel, along with insets of the electron micrographs along the lateral and the longitudinal directions.

In vitro cytotoxicity determined using MTT assay method showed that both the chitosan and *ex situ* prepared colloidal ferric salts (ferric hydroxide and ferric phosphate) had very low cytotoxicity, at all concentrations measured, viz. 0.1, 0.5 and 1 mg/ml. Interestingly, this cell viability increased with incubation time, with the maximum at 72 hours, in almost all the cases. This indicates the proliferation of the cells, brought about by the attachment to and growth on the surface. Likewise, both the neutralized and non-neutralized gels gave cell viability around 80 %, at all concentrations, which increased with incubation time. Being very similar in cytotoxicity to chitosan, these crosslinked gels may be utilized as scaffolds for tissue engineering, either as an injectable or as a preformed product. These cytotoxicity results are presented in Figures S48-S52.

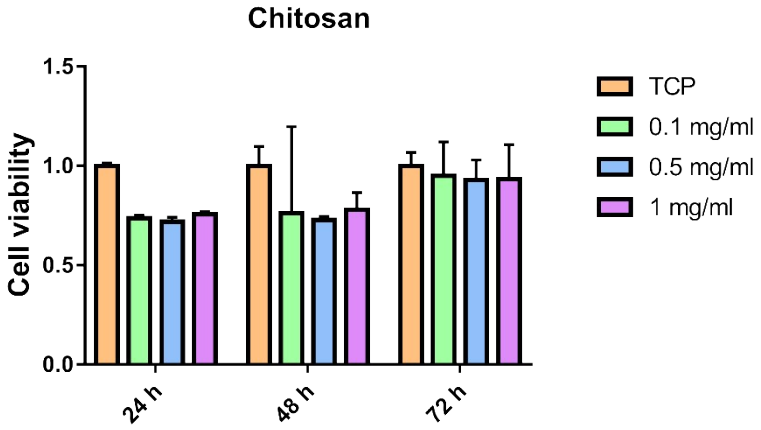

Figure S48. *In vitro* cytotoxicity for chitosan by MTT assay.

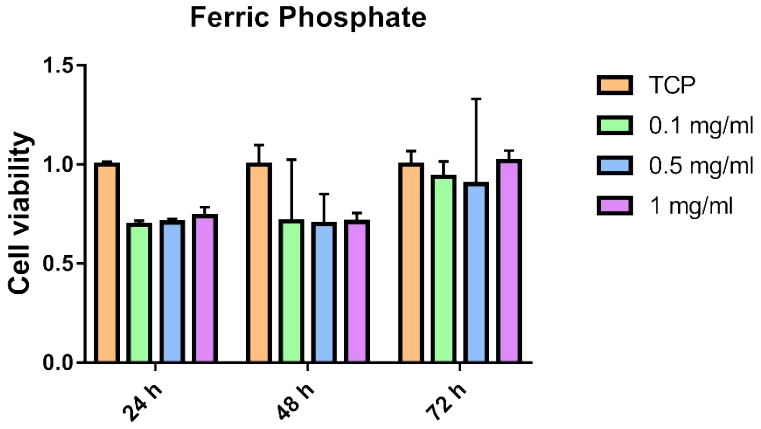

Figure S49. *In vitro* cytotoxicity for ferric phosphate by MTT assay.

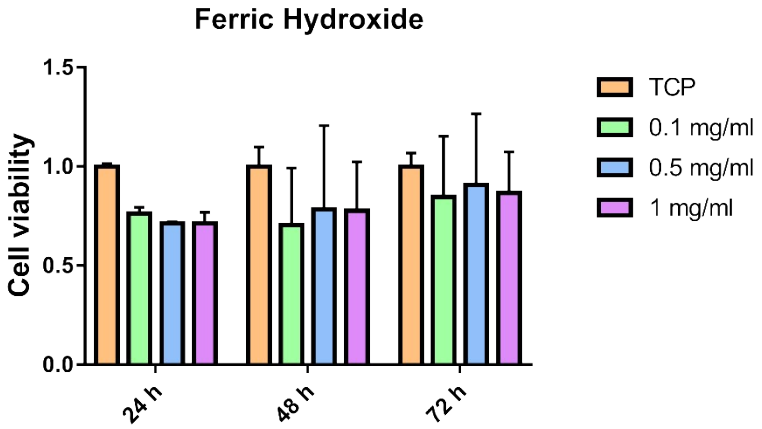

Figure S50. *In vitro* cytotoxicity for ferric hydroxide, which is produced during neutralization, by MTT assay.

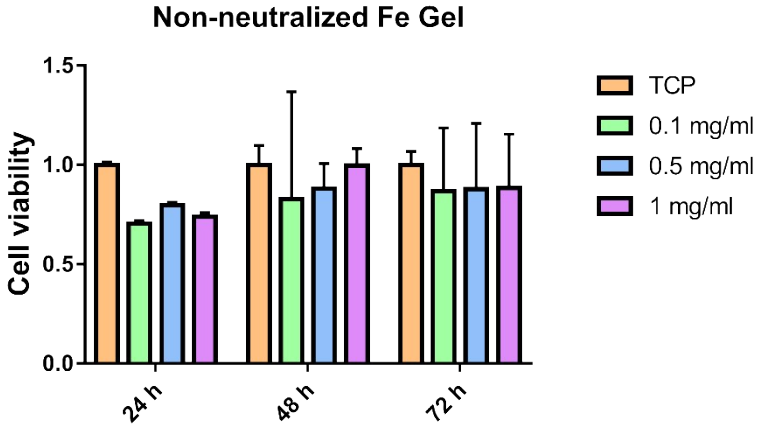

Figure S51. *In vitro* cytotoxicity for neutralized ferric-based gel by MTT assay.

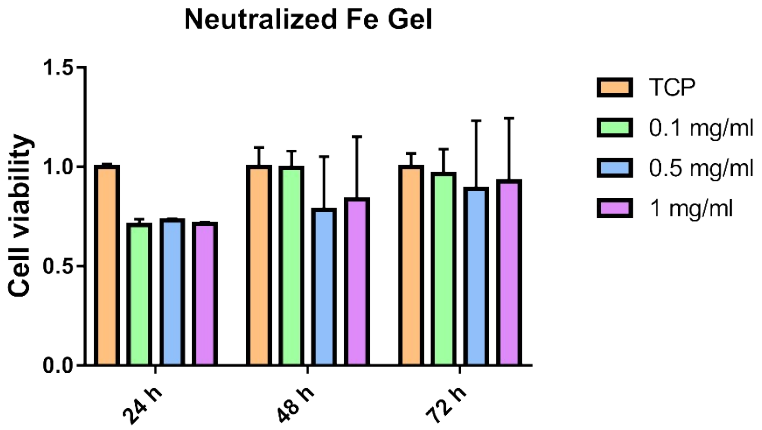

Figure S52. *In vitro* cytotoxicity for non-neutralized ferric-based gel by MTT assay.

The cell attachment studies showed that the surface of the scaffold is highly conducive for the growth of the cells. Under SEM, cells were observed to have attached well to the surface and proliferated, whilst the morphology of the gel was maintained. Few SEM and fluorescence micrographs are presented in Figures S53. DAPI is a fluorescent stain strongly binds to A – T rich regions present in DNA. From the fluorescence micrographs, presented in Figure S54, it is clear that the nuclear integrity of the attached cells was unaffected.

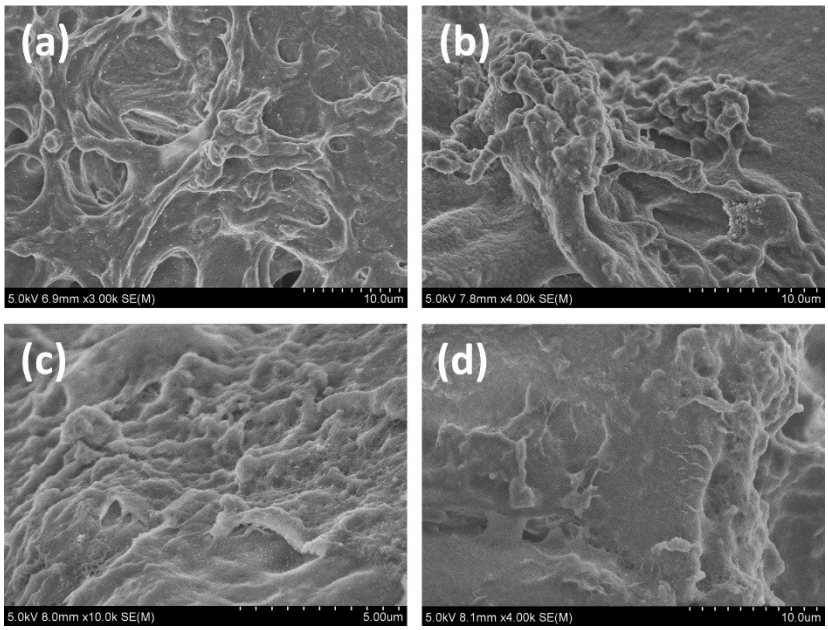

Figure S53. SEM micrographs, showing the cell attachment and proliferation of NIH 3T3 mouse fibroblast cells.

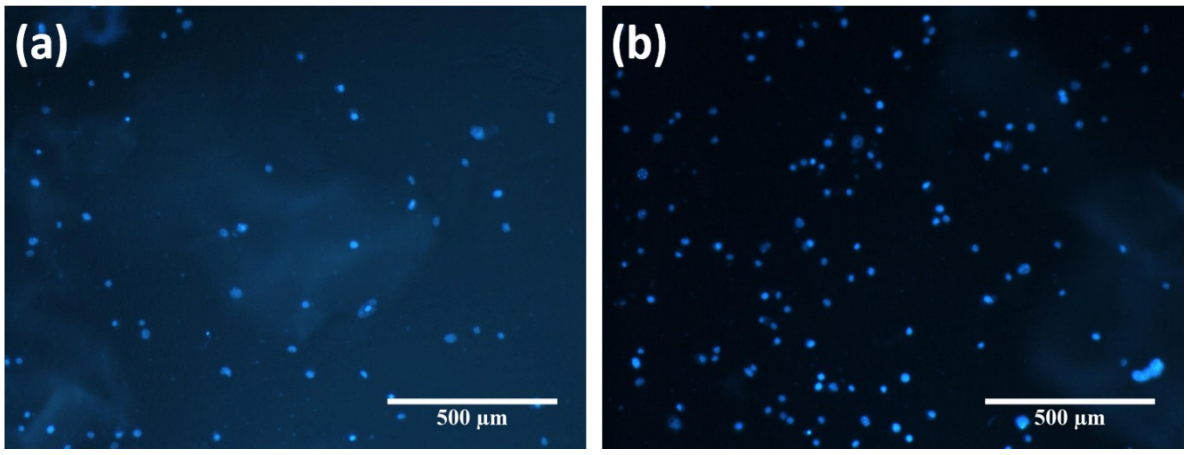

Figure S54. Fluorescence micrographs, showing the cell attachment and proliferation of NIH 3T3 mouse fibroblast cells, after DAPI staining.

In order to improve the antimicrobial nature, the ferric-based gel was washed extensively with 0.1 M NaOH. Apart from neutralization of chitosan, which produces free amine groups on the chitosan backbone, phosphate ions in the metal colloids were found to exchange with hydroxyl ions, leading to the formation of metal hydroxides. Interestingly, this transformation did not affect the stability of the gel. While the photographs of the agar plates which show antimicrobial activity are presented in Figures S55-S57. The measured inhibition zones for various samples are given in Tables S4-S7.

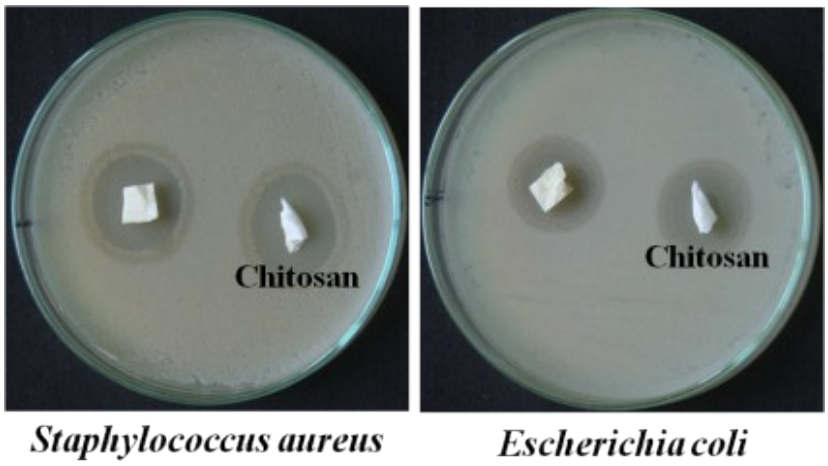

Figure S55. Antimicrobial activity for chitosan.

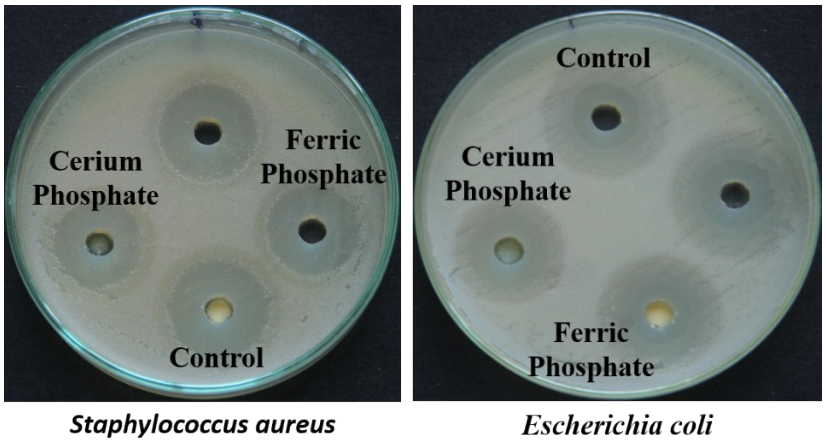

Figure S56. Antimicrobial activity for various colloidal metal salts.

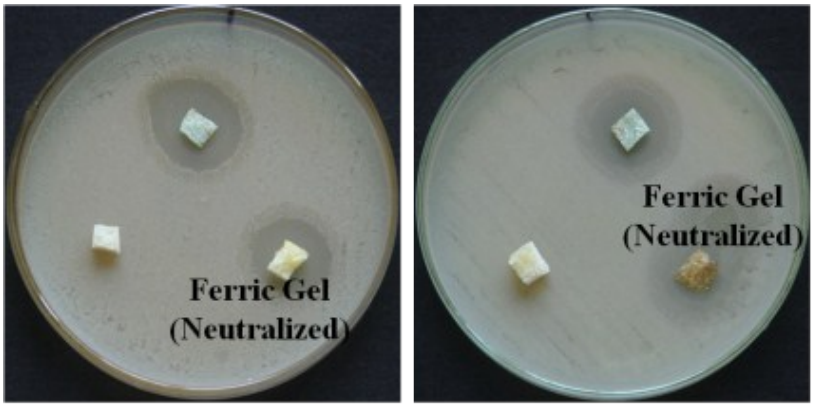

Figure S57. Antimicrobial activity for neutralized ferric-based gel.

Table S4. Antimicrobial activity for chitosan.

Name of the Pathogen	Inhibition Zone (mm)
Staphylococcus aureus (+ve)	18
Escherichia coli (-ve)	18

Table S5. Antimicrobial activity for few colloidal metal salts (100µl of 4.67 wt. % (50 mg in 1 ml) aqueous dispersion).

Name of the Pathogen	Inhibition Zone (mm)	
	Ceric Phosphate	Ferric Phosphate
Staphylococcus aureus (+ve)	18	18
Escherichia coli (-ve)	20	21

Table S6. Antimicrobial activity for ferric-based gel (Non-neutralized and Neutralized).

Name of the Pathogen	Inhibition Zone (mm)	
	Ferric-based Gel (Non-neutralized)	Ferric-based Gel (Neutralized)
Staphylococcus aureus (+ve)	-	18
Escherichia coli (-ve)	-	23

Table S7. Antimicrobial activity for control (streptomycin; 1000 μg in 1 ml).

Name of the Pathogen	Inhibition Zone (mm)
Staphylococcus aureus (+ve)	22
Escherichia coli (-ve)	24

Application of cerium-based gel as recoverable, heterogeneous catalyst in aza-Michael addition

The gels reported here and epecially those containing transition and rare-earth metal ions, can be used as recoverable catalysts. As an example, aza-Michael reaction of amines with α,β-unsaturated carbonyl compounds was performed using cerium-based gel as the catalyst. After the reaction, the crude product containing the excess diallylamine (acrylamide had reacted completely) dissolved in water was purified by simple distillation under vacuum. Yield:, 95 %; product was found to be highly pure, as per the detection limit of NMR.

The NMR of the final product gave the following peaks: ^{1}H (400 MHz, DMSO-D6) δ, ppm = 2.23-2.27 **(-CH_2-N< (acrylamide))**, 2.5 **(DMSO-D6)**, 2.69-2.72 **(-CO-CH_2- (acrylamide))**, 3.13-3.14 **(-CH_2- (diallylamine))**, 4.26 **(H_2O)**, 5.15-5.25 **(=CH_2 (diallylamine))**, 5.78-5.85 **(=CH- (diallylamine))**, 6.81 **(-CO-NH (acrylamide))** and 7.39 ppm **(H-bonded NH (acrylamide))**. ^{13}C (400 MHz, DMSO-D6) δ, ppm = 32.3 **(-CH_2-N< (acrylamide))**, 38.9-40.1 **(DMSO-D6)**, 48.8 **(-CO-CH_2- (acrylamide))**, 55.6-55.7 **(-CH_2- (diallylamine))**, 118.6 **(=CH_2 (diallylamine))**, 134.4 **(=CH- (diallylamine))** and 173.2 ppm **(>C=O (acrylamide))**. Clearly, the peaks corresponding to C=C in acrylamide disappears, while new peaks, corresponding to

-CH_2-CH_2- appear, confirming the formation of aza-Michael adduct between diallylamine and acrylamide to form 3-(diallylamino)propanamide. The formation of the adduct was further confirmed by HR-ESI mass spectrometry, wherein a new peak at 169.1359 Da was observed, due to the protonated 3-(diallylamino)propanamide. Hence, these gel systems, especially those of transition metals and rare-earths, can be used as recoverable catalysts. The ^{1}H, ^{13}C, DEPT, COSY, HSQC, HMBC NMR spectra and the HRMS spectra of the final product are presented in Figures S58-S64.

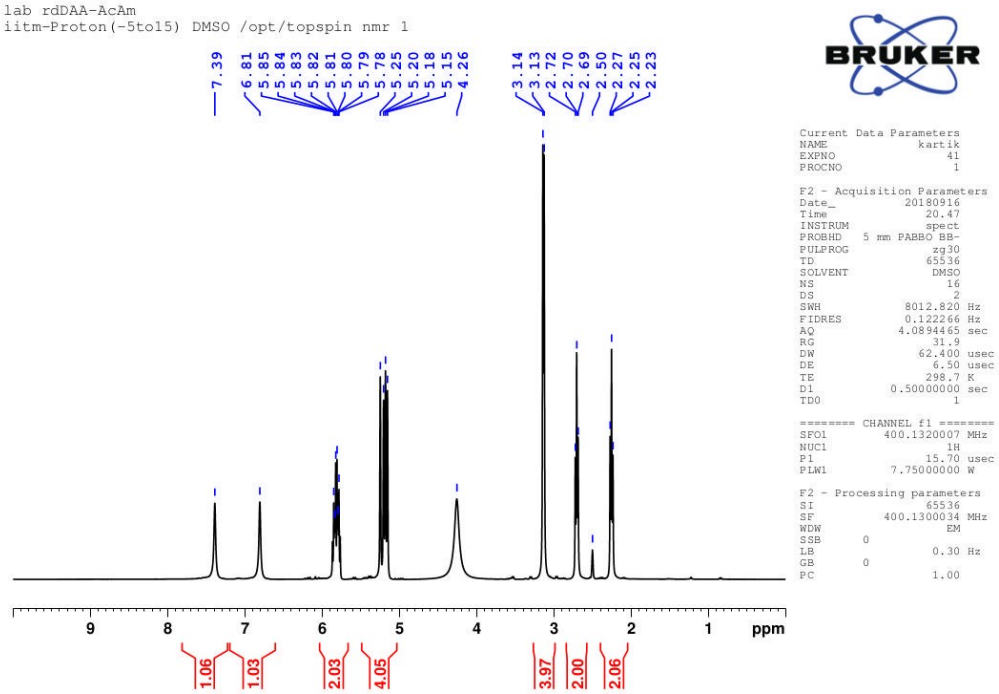

Figure S58. ^{1}H NMR spectrum for the aza-Michael adduct.

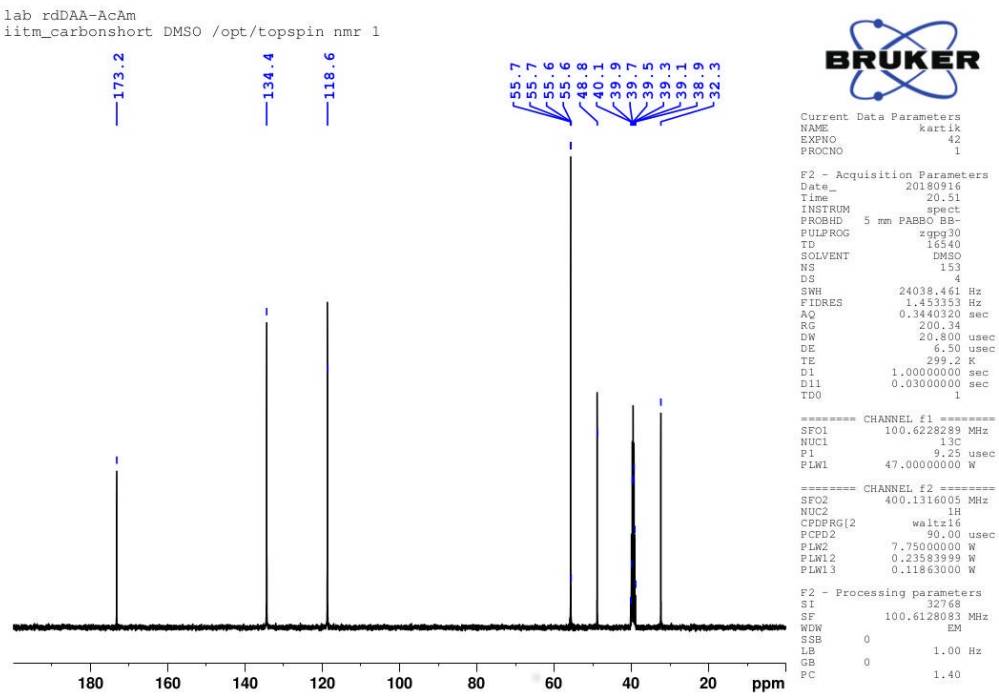

Figure S59. ^{13}C NMR spectrum for the aza-Michael adduct.

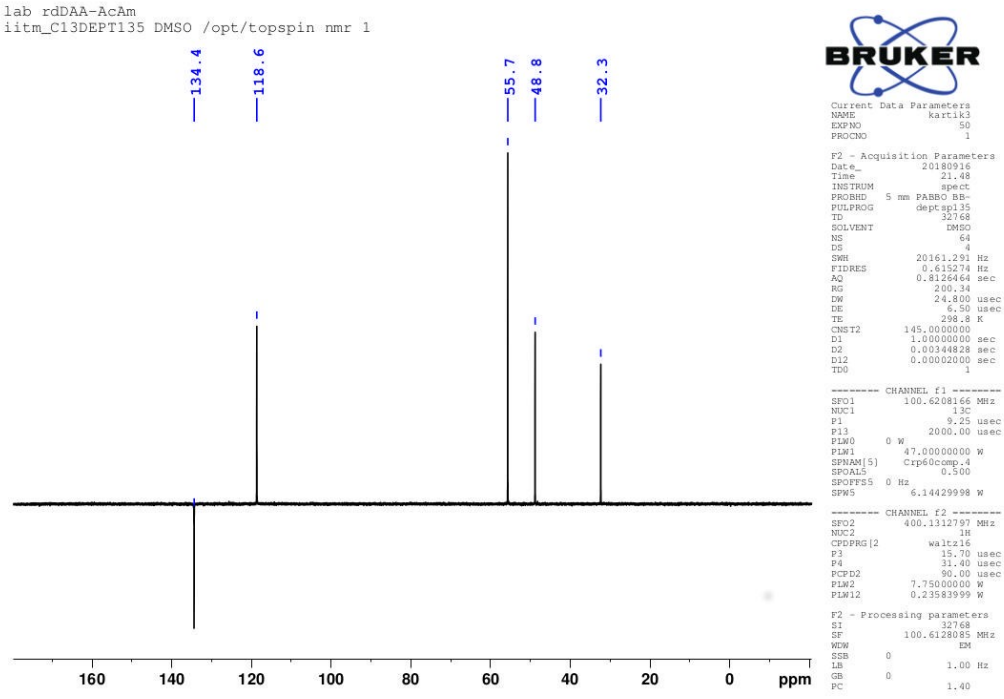

Figure S60. DEPT NMR spectrum for the aza-Michael adduct.

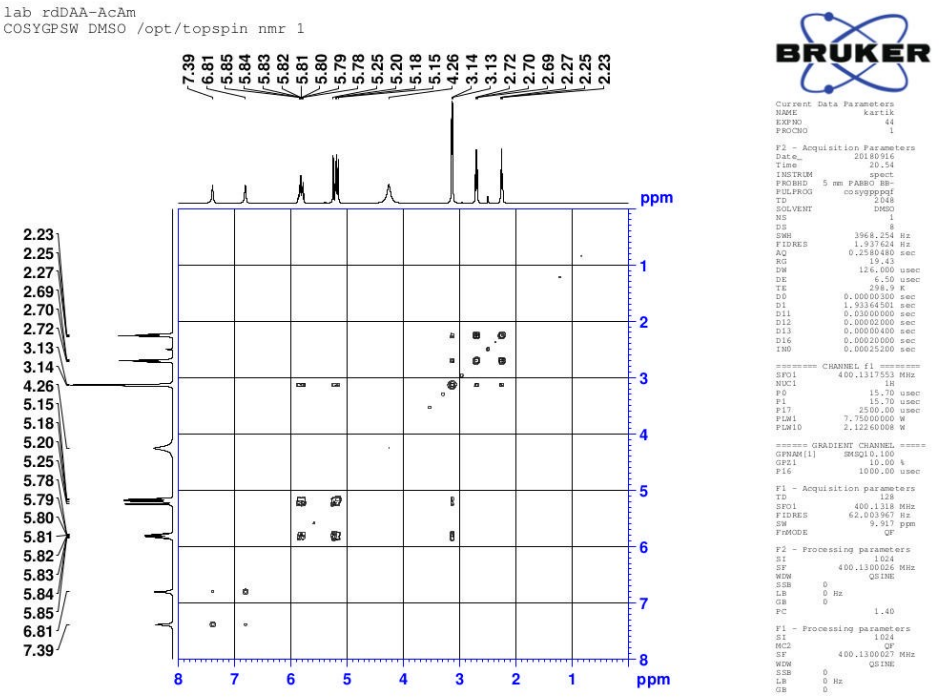

Figure S61. COSY NMR spectrum for the aza-Michael adduct.

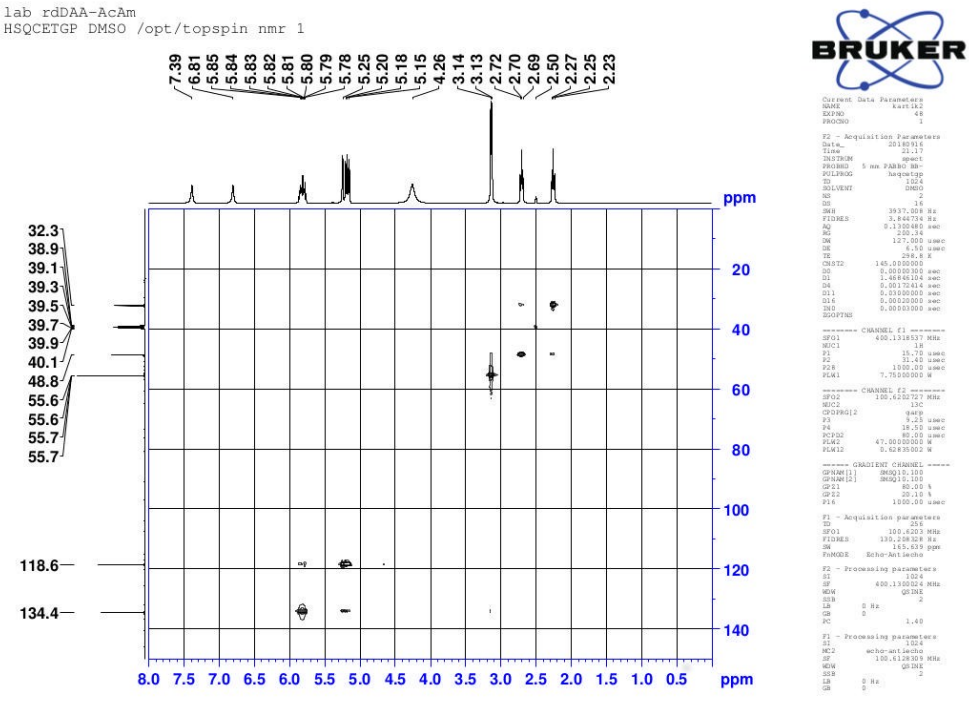

Figure S62. HSQC NMR spectrum for the aza-Michael adduct.

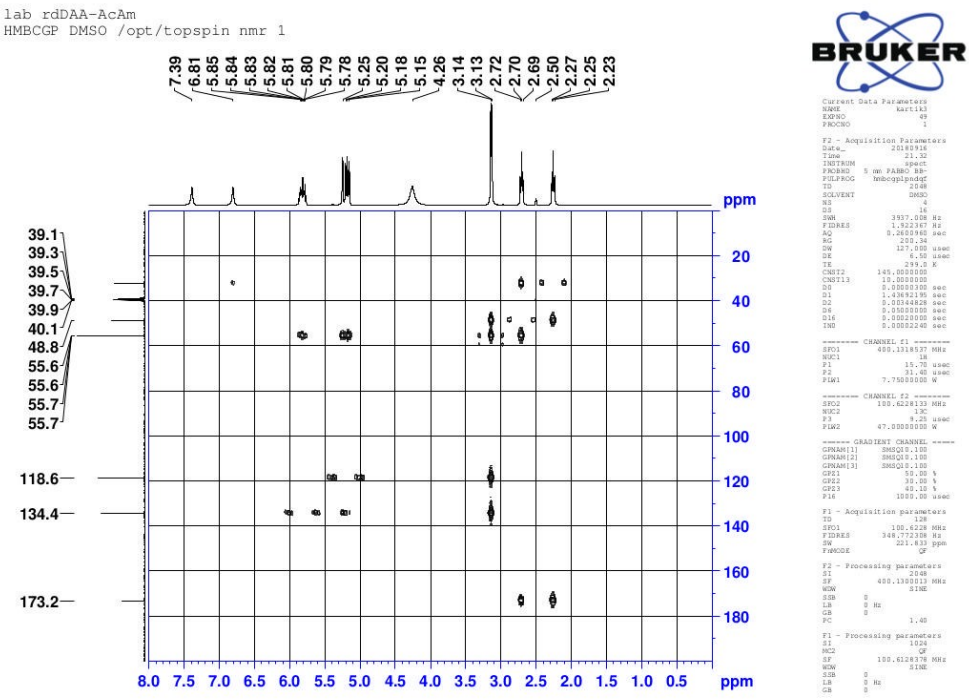

Figure S63. HMBC NMR spectrum for the aza-Michael adduct.

Elemental Composition Report **Page 1**

Single Mass Analysis
Tolerance = 5.0 mDa / DBE: min = -1.5, max = 50.0
Element prediction: Off
Number of isotope peaks used for i-FIT = 3

Monoisotopic Mass, Odd and Even Electron Ions
12 formula(e) evaluated with 1 results within limits (up to 50 best isotopic matches for each mass)
Elements Used:
C: 0-9 H: 0-17 N: 0-2 O: 0-1 K: 0-1
RD-DAA-ACAM
17092018-06-RD-DAA-ACAM 61 (1.534) AM (Cen,5, 80.00, Ar,5000.0,0.00,1.00); Sb (1,40.00); Sm (Mn, 1x5.00); Cm (38:61) TOF MS ES+
4.72e+005

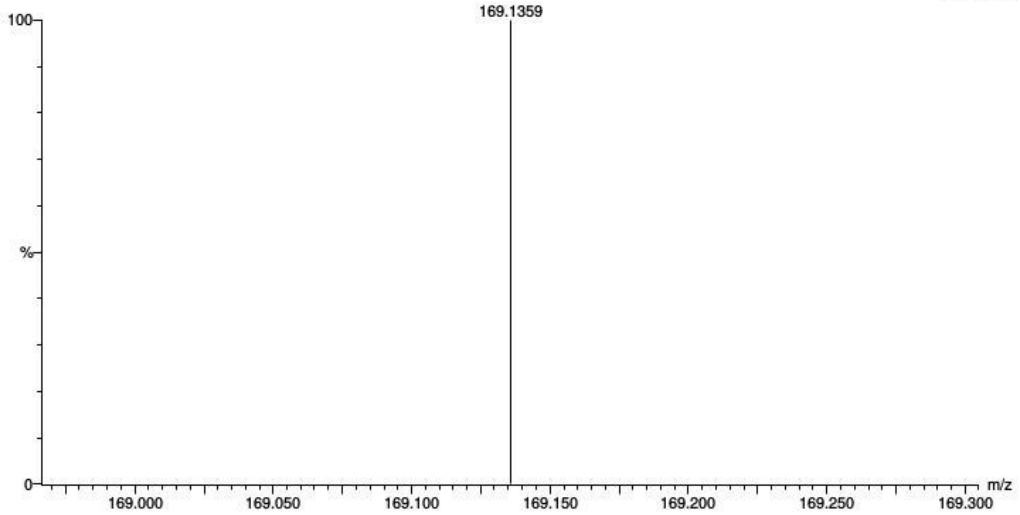

Minimum:				-1.5		
Maximum:		5.0	10.0	50.0		
Mass	Calc. Mass	mDa	PPM	DBE	i-FIT	Formula
169.1359	169.1341	1.8	10.6	2.5	n/a	C9 H17 N2 O

Figure S64. HRMS spectrum for the aza-Michael adduct.

Given the hydrophilic nature of these gels, their water absorption was analyzed. For these measurements, the ferric-based gel was considered as the model, due to its low cost and optimal mechanical properties. The ferric-based gel showed a water absorption of 84 g per g (g/g). In saline solution (0.9 wt. % NaCl), the water absorption dropped to ~ 36 g/g. This decrease in the water absorption indicated that the initial water absorption was primarily due to ionic groups ($-NH_3^+$) on the chitosan backbone, which draws the water into the crosslinked matrix. However, under load, the saline water absorption reduced dramatically from 36 g/g to ~ 2.5 g/g. Additionally, these non-neutralized ferric phosphate-based gels did not show any antimicrobial nature, possibly due to the absence of free amine groups on the chitosan backbone. It may be noted that the colloidal ferric phosphates itself were of low cytotoxicity at low to medium concentrations.

Neutralized ferric-based gels gave a water absorption of ~ 20 g/g for both the distilled and saline water, indicating that the mechanism of water absorption is purely capillary. However, we could not find any interconnected porous structure, when observed under SEM. We, hence, hypothesize that the amorphous region is primarily involved in the water absorption. Further confirmation arises from the x-ray diffractometry measurements, which showed the formation of fully amorphous chitosan, upon gelation. Under load, the saline water absorption reduced dramatically from 20 g/g to ~ 5 g/g, which is comparable to the commercial absorbents used in the commercial sanitary napkins. Since neutralization produced many free amine groups on the chitosan backbone, this neutralized ferric-based gel also gave good antimicrobial activity against *Staphylococcus aureus* and *Escherichia coli*. These gels have a very good potential for replacing present absorbents in sanitary napkins, whilst providing antimicrobial activity without any external additives. The apparatus for testing of AUL is presented in Figure S65, while the water absorption plots under various conditions are presented in Figures S66-S70.

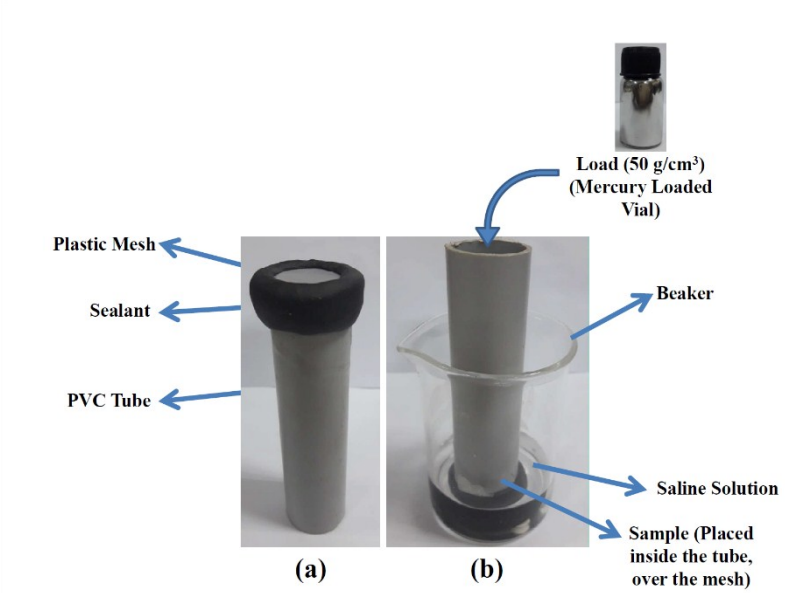

Figure S65. In-house set-up used to compare AUL for different materials.

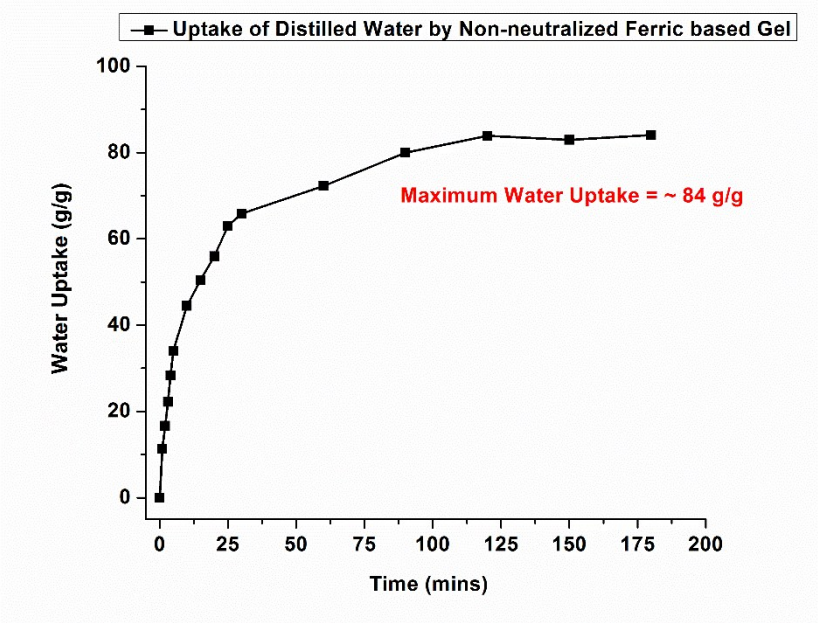

Figure S66. Absorption of distilled water by non-neutralized ferric-based gel.

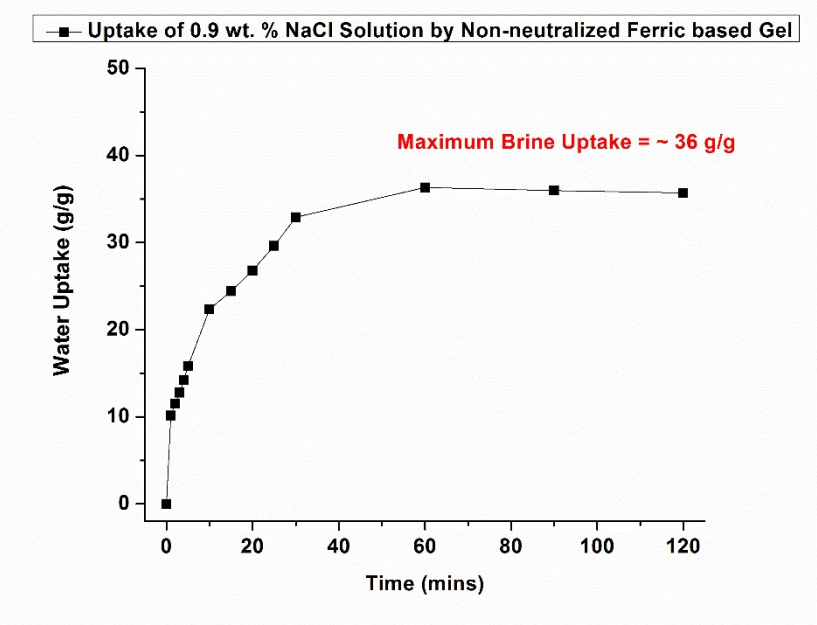

Figure S67. Absorption of saline water by non-neutralized ferric-based gel.

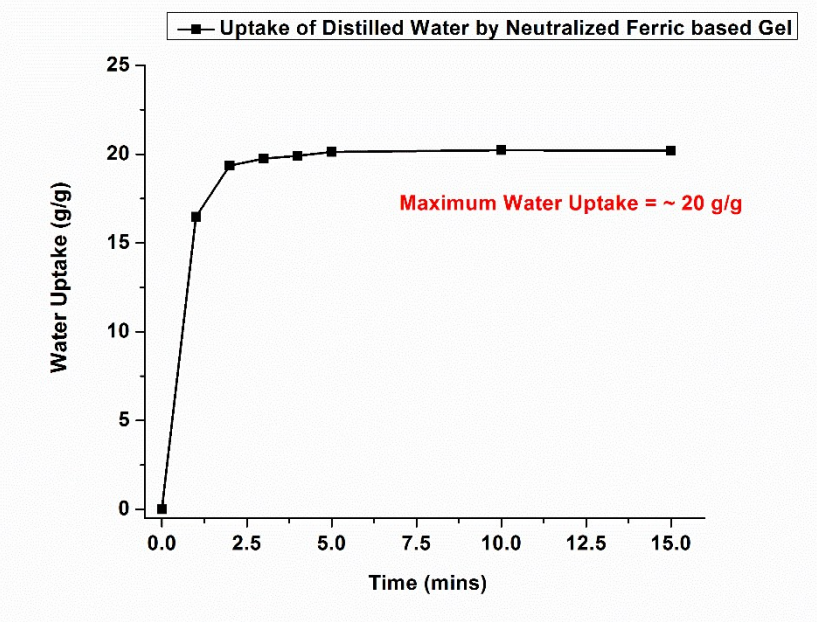

Figure S68. Absorption of distilled water by neutralized ferric-based gel.

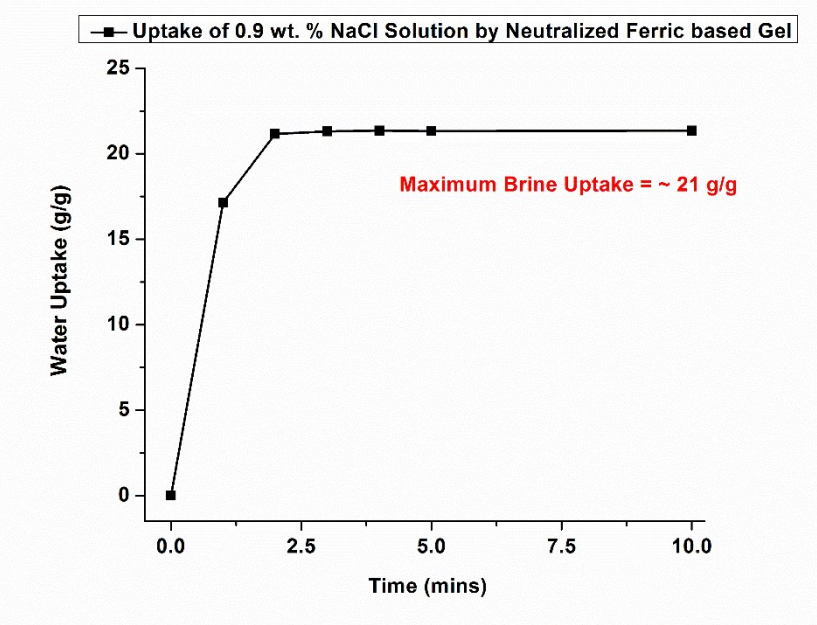

Figure S69. Absorption of saline water by neutralized ferric-based gel.

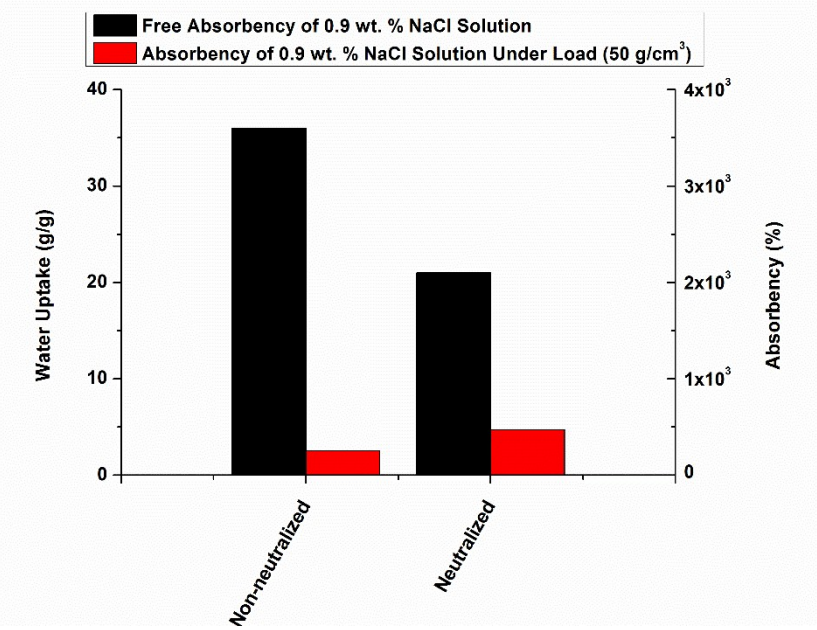

Figure S70. Comparison of absorbency with (AUL) and without load for saline water.

III. References

1 S. J. Lee, J. J. Yoo, G. J. Lim, A. Atala and J. Stitzel, *J. Biomed. Mater. Res. Part A*, 2007, **83A**, 999–1008.

2 B. Chazotte, *Cold Spring Harb. Protoc.*, 2011, **2011**, pdb.prot5556.

3 E. Hatzakis and P. Dais, *J. Agric. Food Chem.*, 2008, **56**, 1866–1872.

4 A. E. Wroblewski, K. Reinartz and J. G. Verkade, *Energy and Fuels*, 1991, **5**, 786–791.

5 D. C. Braddock, J. Clarke and H. S. Rzepa, *Chem. Commun. (Camb).*, 2013, **49**, 11176–8.

6 H. Nakayama, T. Eguchi, N. Nakamura, S. Yamaguchi, M. Danjyo and M. Tsuhako, *J. Mater. Chem.*, 1997, **7**, 1063–1066.

7 N. N. Hirokazu Nakayama, Aki Hayashi, Mitsutomo Tsuhako, Taro Eguchi, H. Nakayama, A. Hayashi, M. Tsuhako, T. Eguchi and N. Nakamura, *Phosphorus Res. Bull.*, 1998, **8**, 89–94.

8 S. Supper, N. Anton, N. Seidel, M. Riemenschnitter, C. Schoch and T. Vandamme, *Langmuir*, 2013, **29**, 10229–10237.

9 L. Heux, J. Brugnerotto, J. Desbrières, M.-F. F. Versali, M. Rinaudo, J. Desbrieres, M.-F. F. Versali and M. Rinaudo, *Biomacromolecules*, 2000, **1**, 746–751.

10 R. Glemza, Y. O. Parent and W. A. Welsh, *Catal. Today*, 1992, **14**, 175–188.

11 C. N. R. R. S Prabakar, KJ Rao, S. Prabakar, K. J. Rao and C. N. R. Rao, *Mater. Res. Bull.*, 1991, **26**, 805–812.

12 R. Lookman, P. Grobet, R. Merckx and W. H. Van Riemsdijk, *Geoderma*, 1997, **80**, 369–388.

13 H. Yi, L. Q. Wu, W. E. Bentley, R. Ghodssi, G. W. Rubloff, J. N. Culver and G. F. Payne, *Biomacromolecules*, 2005, **6**, 2881–2894.